Carbohydrate Polymers 292 (2022) 119638

Contents lists available at ScienceDirect

Carbohydrate Polymers

journal homepage: www.elsevier.com/locate/carbpol

Highly elastic and bioactive bone biomimetic scaffolds based on platelet lysate and biomineralized cellulose nanocrystals

João P. Ribeiro [a,b], Rui M.A. Domingues [a,b], Pedro S. Babo [a,b], Liebert P. Nogueira [c], Janne E. Reseland [d], Rui L. Reis [a,b], Manuel Gomez-Florit [a,b,*,1], Manuela E. Gomes [a,b]

[a] 3B's Research Group, I3Bs — Research Institute on Biomaterials, Biodegradables and Biomimetics, University of Minho, Headquarters of the European Institute of Excellence on Tissue Engineering and Regenerative Medicine, AvePark, Parque de Ciência e Tecnologia, Zona Industrial da Gandra, 4805-017 Barco, Guimarães, Portugal

[b] ICVS/3B's — PT Government Associate Laboratory, Braga, Guimarães, Portugal

[c] Oral Research laboratory, Faculty of Dentistry, University of Oslo, Norway

[d] Department of Biomaterials, Faculty of Dentistry, University of Oslo, Norway

ARTICLE INFO

Keywords:
Nanoscale biomineralization
Cryogels
Cellulose nanocrystals
Calcium phosphate
Hydroxyapatite
Non-collagenous proteins
Platelet lysate

ABSTRACT

Bone is a vascularized organic-inorganic composite tissue that shows a heavily-mineralized extracellular matrix (ECM) on the nanoscale. Herein, the nucleation of calcium phosphates during the biomineralization process was mimicked using negatively-charged cellulose nanocrystals (CNCs). These mineralized-CNCs were combined with platelet lysate to produce nanocomposite scaffolds through cryogelation to mimic bone ECM protein-mineral composite nature and take advantage of the bioactivity steaming from platelet-derived biomolecules. The nanocomposite scaffolds showed high microporosity (94–95%), high elasticity (recover from 75% strain cycles), injectability, and modulated platelet-derived growth factors sequestration and release. Furthermore, they increased alkaline phosphatase activity (up to 10-fold) and up-regulated the expression of bone-related markers (up to 2-fold), without osteogenic supplementation, demonstrating their osteoinductive properties. Also, the scaffolds promoted the chemotaxis of endothelial cells and enhanced the expression of endothelial markers, showing proangiogenic potential. These results suggest that the mineralized nanocomposite scaffolds can enhance bone regeneration by simultaneously promoting osteogenesis and angiogenesis.

1. Introduction

Bone is a composite material whose extracellular matrix (ECM) consists mostly of type I collagen fibrils co-assembled with non-collagenous proteins and apatite nanocrystals that form a highly complex and organized scaffold (Nudelman et al., 2010; Reznikov, Steele, Fratzl, & Stevens, 2016). At ultrastructural level, these nanocrystals, have a platelet-shaped form and are hierarchically allocated both within and between the collagen fibers, providing bone with outstanding load-bearing function (Reznikov, Bilton, Lari, Stevens, & Kröger, 2018). During bone biomineralization, mineral precursor ions are sequestered to form metastable nanodroplets of amorphous calcium phosphate (CaP), which penetrate the interstices of collagen fibrils, later transforming into thermodynamically stable hydroxyapatite (HAp) crystals (Gorski, 2011; Yu & Wei, 2021). This nanoscale biomineralization process is regulated by matrix non-collagenous proteins (NCPs), among other factors (Nudelman et al., 2010). NCPs, such as osteocalcin (OC) and osteopontin (OPN), are anionic ECM proteins that play an active role on the formation of negatively charged complexes of mineral precursors, which enter collagen fibrils through electrostatic interactions and allow the intrafibrillar collagen mineralization (Yu & Wei, 2021). Actually, recent works have used NCPs or NCPs-mimetic polymers to promote nanoscale mineralization, which has positively influenced the osteogenic differentiation of stem cells (Niu et al., 2016; Thrivikraman et al., 2019; Ye et al., 2021).

Bone defects caused by trauma, tumor excision, or pathologic bone

* Corresponding author at: 3B's Research Group, I3Bs – Research Institute on Biomaterials, Biodegradables and Biomimetics, University of Minho, Headquarters of the European Institute of Excellence on Tissue Engineering and Regenerative Medicine, AvePark, Parque de Ciência e Tecnologia, Zona Industrial da Gandra, 4805-017 Barco, Guimarães, Portugal.

E-mail address: manuel.gomezflorit@ssib.es (M. Gomez-Florit).

[1] Present address: Health Research Institute of the Balearic Islands (IdISBa), 07010 Palma, Spain.

https://doi.org/10.1016/j.carbpol.2022.119638
Received 25 February 2022; Received in revised form 29 April 2022; Accepted 16 May 2022
Available online 20 May 2022
0144-8617/© 2022 The Authors. Published by Elsevier Ltd. This is an open access article under the CC BY-NC-ND license (http://creativecommons.org/licenses/by-nc-nd/4.0/).

resorption affect and limit patients aesthetically and functionally, reducing their quality of life. In the case of critical-size defects, the gold standard for bone reconstruction is the use of autologous or allogenic bone grafts (Wang & Yeung, 2017). Nevertheless, their use presents major drawbacks including discomfort, pain, invasive harvesting, risk of donor site morbidity, and limited functional and aesthetic recovery (Osborn, Helal, & Mehra, 2018; Wang & Yeung, 2017). On the other hand, allografts can induce disease transmission and immune rejection (Wang & Yeung, 2017). Over the past decades, several tissue engineering and regenerative medicine (TERM) approaches have been proposed for bone regeneration (Koons, Diba, & Mikos, 2020; Pina, Oliveira, & Reis, 2015). Typically, they rely on the combination of inorganic (CaP or ceramics) and/or organic (synthetic or natural origin polymers) biomaterials-based scaffolds, progenitor cells, and biophysical/biochemical stimuli, which have demonstrated some level of success on promoting bone regeneration (Koons et al., 2020; Pina et al., 2015). This has been mainly attributed to the release of osteoinductive calcium and phosphate ions from CaP (Chahal et al., 2020; Koons et al., 2020; Tang, Li, Tan, Fan, & Zhang, 2018). However, the most commonly used CaP forms are crystalline, such as HAp, which are stable under physiological conditions, exhibit slow release of ions and fail to mimic the nanoscale biomineralization process. On the other hand, although amorphous CaP forms show lower stability and higher release of bioactive ions, they spontaneously transform into thermodynamically favourable crystalline phases, which require stabilization before their incorporation in composite scaffolds (Bjørnøy et al., 2016; Schweikle et al., 2019).

Naturally occurring cellulose nanocrystals (CNCs) have been extensively applied in TERM strategies as nanofillers, crosslinking agents, and as templates for the design of a wide range of new biomaterials due to their high mechanical strength, biocompatibility, low density, high aspect ratio and surface area, and convenient surface chemistry (Domingues, Gomes, & Reis, 2014). Moreover, their typical production process results in a negative surface charge that improves their colloidal stability (Moon, Martini, Nairn, Simonsen, & Youngblood, 2011). Particularly, as templates, CNCs are an outstanding support for loading inorganic nanoparticles (e.g. Ag, Au, Pt, Pd), producing stable organic-inorganic nanocomposite nanoparticles in aqueous media (Islam, Chen, Sisler, & Tam, 2018). In this sense, CNCs, among other cellulosic materials, have been exploited as templates for the growth of inorganic CaP in situ (Bharadwaz & Jayasuriya, 2020; Khan et al., 2021; Torgbo & Sukyai, 2018). This type of nanocomposites has been used as micrometric coatings for scaffolds or cell culture plates, as culture media supplements, and as scaffold precursors for bone tissue engineering (Fragal et al., 2016, 2019; Huang et al., 2019; Ishikawa et al., 2015; Kumar, Negi, Choudhary, & Bhardwaj, 2014). Nevertheless, these strategies poorly mimic how minerals components are embedded in the bone ECM structure.

We have previously modified CNCs with aldehyde groups (a-CNCs) to increase the crosslinking of low strength matrices, such as hyaluronic acid or platelet lysate (PL), obtaining hydrogels mimicking the ECM of native tissues (Mendes, Gómez-Florit, Babo, et al., 2018; Silva et al., 2018). Actually, PL is a safe, cost-effective, and easily standardized liquid blood derivative prepared from clinical-standard platelet concentrates rich in bioactive (e.g. growth factors (GFs), cytokines) and self-assembling structural proteins, among others, which has been used to produce various types of hydrogels and scaffolds for different TERM strategies or as alternative culture supplement to fetal bovine serum (Mendes, Gómez-Florit, Babo, et al., 2018). In addition, PL has shown to be capable of enhancing stem cells recruitment, angiogenesis, and osteogenesis (Chahal, Gómez-Florit, Domingues, Gomes, & Tiainen, 2021; Silva et al., 2018; Tavares et al., 2021; Zhang et al., 2021). For instance, the incorporation of PL into hyaluronic acid (HA) microparticles enhanced the biological performance and osteogenic potential of CaP cements through the sustained release of PL chemotactic and osteogenic GFs (Babo, Santo, Gomes, & Reis, 2016).

In this work, bioinspired by the role of negatively charged NCPs in the formation of apatite crystals in bone, we aimed to mimic their function using negatively charged CNCs to obtain mineralized CNCs (m-CNCs). We hypothesized that scaffolds composed of PL reinforced and crosslinked with a-CNCs and including m-CNCs would mimic the nanoscale biomineralization microenvironment while acting as a stable three-dimensional (3D) network and locally delivering the biologically relevant PL-derived proteins to promote the osteogenic differentiation of progenitor/stem cells. The scaffolds and its precursors were thoroughly characterized regarding their chemical, morphological, microstructural, and mechanical properties, as well as their swelling and degradation profiles. The biological performance, particularly the osteoinductive potential, of the developed cryogel scaffolds was evaluated using human adipose tissue-derived stem cells (hASCs). For this, the impact of the mineralized cryogel scaffolds on cells proliferation, metabolic activity and differentiation was assessed. Moreover, considering that bone is a vascularized tissue, we assessed the potential of our scaffolds to promote the recruitment of endothelial cells and support angiogenesis.

2. Materials and methods

2.1. Production of cryogels precursors

2.1.1. Synthesis and aldehyde functionalization of CNCs

CNCs were isolated from microcrystalline cellulose (MCC, Sigma-Aldrich, USA), following a well-established sulfuric acid hydrolysis method described by Bondeson et al. and adapted by Domingues et al. (Bondeson, Mathew, & Oksman, 2006; Domingues et al., 2015). Then, aldehyde-modified CNCs (a-CNCs) were produced through sodium periodate ($NaIO_4$) oxidation route, according to the procedures described elsewhere with minor modifications (Domingues et al., 2015; Kim, Kuga, Wada, Okano, & Kondo, 2000). Further details on synthesis and characterization of produced CNCs is provided in Supporting Information.

2.1.2. CNCs mineralization

m-CNCs production was inspired by previously reported synthesis strategies (Ishikawa et al., 2015) with the required modifications for the proposed application. In brief, a simplified simulated body fluid (s-SBF) solution composed of 140.0 mM sodium chloride (NaCl, Honeywell, USA), 2.5 mM calcium chloride hexahydrate ($CaCl_2.6H_2O$, Sigma-Aldrich, USA), 1.0 mM disodium hydrogen phosphate (Na_2HPO_4, 98%, abcr GmbH, Germany), and 20 mM hydrochloric acid (HCl, VWR, France) was prepared 24 h in advance, and stored at RT preventing from air and light exposure to avoid undesired precipitation. Thereafter, different volumes of CNCs aqueous solution (0.8 wt%) were added to s-SBF to obtain a final volume of 1 L with molar ratio of calcium ions (in s-SBF) to sulfate groups (in CNCs surface) (Ca^{2+}/SO_3^-) of 10:1, 20:1, and 40:1. The suspension was then first vigorously stirred and then moved to an ultrasonic water bath (DT 100H Sonorex Digitec, Bandelin, Germany) for 30 min to ensure even dispersion. Afterwards, the pH of the mixture was adjusted to two different values, 6.9 and 7.9, with the addition of tris(hydroxymethyl)aminomethane (Trisbase, Alfa Aesar, Germany). After this, the solutions were placed in an orbital/linear thermostatic shaking water bath (OLS 200, Grant, UK) at 37 °C and 150 rpm for 1 h. The ultrasound and shaking cycles were repeated three times. Subsequently, the precipitated products were collected by centrifugation (Eppendorf 5810R, Germany) at 3220*g* and 15 °C for 10 min, and washed several times with ethanol and ultrapure water (Milli-Q, 18.2 MΩ.cm) to remove the residual salts. Furthermore, they were dialyzed against ultrapure water for 3 days. Finally, the obtained m-CNCs nanocomposites solutions were stored at 4 °C until further use.

2.1.3. Platelet lysate

PL used in this project was produced from platelet concentrates (PC) obtained from buffy coats, provided by "Serviço de Imunohemoterapia

do Centro Hospitalar de São João" (CHSJ, Porto, Portugal), under an established cooperation protocol, approved by the Hospital Ethical Committee (approval number 363/18). The platelet count was performed at the CHSJ and the sample volume was adjusted to 1 million platelets/mL. PC lots were biologically qualified according to the Portuguese legislation (Decreto-Lei 100/2011) and stored at −80 °C five days after collection. Thereafter, PC lots from ten different donors were subjected to three repeated freeze/thaw cycles (frozen with liquid nitrogen at −196 °C and thawed in a 37 °C water bath), lysing the platelets and releasing their protein content. Then, the cellular debris were removed by centrifugation at 3220*g* for 5 min, and the supernatant was filtered through 0.45 μm sterile filters (TPP, Switzerland).

2.2. Physicochemical characterization of a-CNC and m-CNC

2.2.1. Zeta potential

Surface charge of the different CNCs produced was determined for 0.1% (w/v) suspensions in DI water. Briefly, 1 mL of each suspension was transferred into a Folded Capillary cell (DTS1060, Malvern) and zeta potential was measured by Zetasizer (Nano ZS, Malvern) ($N = 3$).

2.2.2. X-ray diffraction (XRD) analysis

The different CNCs samples were freeze-dried and then pressed on the sample holder to form a uniform layer of material for analysis. The diffraction patterns measurements were performed using a Bragg–Brentano diffractometer (D8 Advance, Bruker, Germany) equipped with Cu Kα radiation. Data sets were collected in the 2θ range of 10–80° with a step size of 0.05° and 1 s for each step, and the obtained diffractograms were processed using OriginPro 2018 software. Subsequently, the average crystallite size was calculated using the Scherrer equation (N = 3) (Bishnoi, Kumar, & Joshi, 2017; Iwashita, 2016).

2.2.3. Scanning electron microscopy (SEM) and energy dispersive spectroscope (EDS) analysis of CNCs

High-resolution SEM (HR-SEM, Auriga Compact, Zeiss, Germany) was used to confirm the successful decoration of CNCs with CaP and to study their morphology. For this purpose, drops of CNCs and m-CNCs dilutions were placed on top of aluminum stubs fitted with conductive adhesive carbon tape (Media Lab System S.r.l., Italy) and circular coverglasses (13 mm Ø; 0.16–0.19 mm thickness; optical quality borosilicate; Agar Scientific Ltd., UK), and allowed to dry until the procedure was performed. After drying, the samples were mounted on the SEM chamber and imaged at RT with an incident electron beam accelerated to 3 kV.

In order to estimate the Ca/P molar ratio of the CaP formed on the surface of CNCs, an EDS detector (INCAx-Act, PentaFET Precision, Oxford Instruments, UK) incorporated in the HR-SEM was used. CNCs and m-CNCs dilutions (0.01 and 0.001% (v/v)) were prepared from the stock solutions and then, a drop of each solution was placed on top of aluminum stubs fitted with conductive adhesive carbon tape (Media Lab System S.r.l., Italy) and tissue coverslips (polyethylene terephthalate, glycol-modified (PET-G); Sarstedt, Germany), and allowed to dry before analysis. After drying, the samples were transferred into the EDS chamber and imaged at RT with an incident electron beam accelerated to 10 kV, and the corresponding the Ca/P molar ratios were calculated for each sample (N = 3).

2.2.4. Thermogravimetric analysis

CNCs samples were freeze-dried, weighted, transferred into platinum pans, and analyzed according to the desired purpose using a simultaneous thermal analyzer (STA7200, Hitachi, Japan) (N = 3). For the determination of the percentage of mineral content, they were heated from 40 °C to 600 °C at 10 °C/min heating rate, after a 2 min isothermal period at 40 °C under a mixture of N_2 and O_2 atmosphere.

2.3. Nanocomposite cryogels production

Nanocomposite cryogel scaffolds were prepared by mixing PL with blends of a-CNCs and m-CNCs at different rations. This mixture was performed by using a double-barrel syringe (1:1 volume ratio) fitted with a static mixer placed at the outlet (Medmix, Germany) to homogenously extrude the cryogel precursor solution into square molds (12 well silicone chamber, Ibidi, Germany). To produce the control cryogel scaffolds (without m-CNCs), barrel A was filled with PL and barrel B with a-CNCs dispersion at 2.4 wt% concentration. For mineralized cryogels, barrel A was also filled with PL wherries barrel B was filled with variable combinations of a-CNCs (1.8–2.4 wt%) and m-CNCs dispersions (0.6–2.4 wt%) to obtain a final nanoparticles concentration of 2.4 wt%. Before extrusion, the viscous a-CNCs suspensions with or without m-CNCs were dispersed with an ultrasonic processor (30 s, 3 cycles, 60% amplitude; VCX750, Sonics & Materials Inc., USA) and sterilized under UV for 30 min. After extrusion into the molds, the cryogel precursors were frozen at −80 °C on top of styrofoam and subsequently freeze-dried until full cryogelation. The final cryogel scaffolds formulations were named according to the type of m-CNCs obtained using different pH (defined after XRD analysis) and their concentrations: 0 wt% (Control), 0.6 wt% m-CNCs 6.9/20 (Amorphous-Low or A-Low), 2.4 wt% m-CNCs 6.9/20 (Amorphous-High or A-High), 0.6 wt% m-CNCs 7.9/20 (Crystalline-Low or C-Low), and 2.4 wt% m-CNCs 7.9/20 (Crystalline-High or C-High).

2.4. Biocompatibility analysis

2.4.1. Human adipose-derived stem cells (hASCs)

hASCs were obtained from lipoaspirate samples of the abdominal region of healthy donors undergoing plastic surgery under the scope of an established protocol with Hospital da Prelada (Porto, Portugal) and with the approval of the Hospital Ethics Committee (approval number 005/2019). The hASC isolation was performed using a previously optimized protocol (Carvalho et al., 2011). hASCs were maintained in complete α-MEM (Sigma-Aldrich) – supplemented with 10% fetal bovine serum (FBS, ThermoFisher Scientific, USA) and 1% antibiotic/antimycotic (A/A, ThermoFisher Scientific) – and incubated at 37 °C in a 5% CO_2 high-humidity environment, with medium replacements every 2 to 3 days. hASCs (1.5×10^5) in 200 μL of media were seeded on the cryogel scaffolds (100 μL on each side). Cells until passage 5 were used for this study.

2.4.2. Live/Dead assay

After 4 days of culture, samples seeded with hASCs (1.5×10^5) were gently rinsed with PBS, incubated with Calcein AM (Invitrogen, USA) 1:500 v/v in PBS for 30 min at 37 °C and then with PI (Invitrogen) 1:1000 v/v solution in PBS also for 30 min at 37 °C. Lastly, the cryogels were washed again with PBS to minimize background fluorescence and visualized using a confocal microscope (TCS SP8, Leica, Germany) (N = 3).

2.4.3. Metabolic activity

The metabolic activity was quantitatively evaluated by the Alamar Blue assay, according to the manufacturer's instructions. Briefly, at each pre-selected time point, a 10% (v/v) Alamar Blue solution (Bio-Rad, UK) in culture media was replaced the previous culture media for 3 h in standard culture conditions. After incubation, 100 μL of each sample (N = 4) supernatant were collected in triplicate and transferred to a 96-well plate. Background was also included by incubating the Alamar Blue solution in the same conditions but without cells. Thereafter, the absorbance was measured using a microplate reader (Synergy HT, Bio-Tek Instruments, USA) at excitation and emission wavelengths of 570 and 600 nm, respectively.

2.4.4. DNA quantification

Cell proliferation was determined by quantifying the total amount of double-stranded DNA (dsDNA) using Quant-iT™ PicoGreen® dsDNA dsDNA Assay Kit (ThermoFisher Scientific), according to the manufacturer's instructions. Briefly, samples were washed with PBS and then incubated with 1 mL of ultra-pure water for 1 h at 37 °C. After this, samples were frozen at −80 °C and then thawed and sonicated using an ultrasonic processor (VCX-130PB-220, Sonics, USA) for 3 cycles of 5 s, to fully lyse the cells and guarantee that all cell content was released. The fluorescence readings were performed in triplicate for each sample (N = 4) in 96-well white plates. The fluorescence was measured using a microplate reader (Synergy HT) at excitation and emission wavelengths of 485/20 and 528/20 nm, respectively. The DNA concentration for each sample was calculated using a standard calibration curve included in the assay.

2.5. Evaluation of the osteogenic differentiation

2.5.1. Alkaline phosphatase activity

Lysed samples (from DNA quantification) were centrifuged at 12,300*g* for 15 min using a microcentrifuge (ScanSpeed Mini, Labogene, Denmark). ALP activity was determined from the supernatant by measuring the hydrolysis of *p*-nitrophenylphosphate (pNPP) in the yellow end-product p-nitrophenol by ALP. For this, 100 μL of pNPP (Sigma-Aldrich) and 20 μL of alkaline buffer solution (Sigma-Aldrich) were added to each sample. The reaction was stopped with 100 μL of 0.3 M NaOH (Panreac Quimica, Spain) and absorbance was measured at 405 nm using a microplate reader (Synergy HT). Four samples of each condition were analyzed (N = 4), and the absorbance readings were performed in duplicate for each sample. The ALP concentration for each sample was calculated from a standard calibration curve included in the assay prepared using a calf intestinal ALP enzyme (1 μmol/min; Promega, USA).

2.5.2. Gene expression

At each time point, the total ribonucleic acid (RNA) from each sample (N = 4) was isolated using TriReagent (Sigma-Aldrich), according to the manufacturer's instructions. After determining the purity and concentration of the extracted RNA by Nanodrop spectrophotometer at 260 nm (Thermo Fisher Scientific), complementary DNA was reverse transcribed using qScript cDNA Synthesis Kit (Quanta biosciences, USA). Aliquots of each cDNA sample were frozen until the polymerase chain reactions (PCRs) were carried out. Real-time PCR was performed in a mastercycler (Realplex, Eppendorf, Germany) using PerfeCTa SYBR Green FastMix (Quanta Biosciences). The amplification program consisted of a pre-incubation step for denaturation of the template cDNA (2 min, 95 °C), followed by 40 cycles of denaturation (5 s, 95 °C), an annealing step (15 s, 60 °C), and an extension step (20 s, 72 °C). Glyceraldehyde-3-phosphate dehydrogenase (GAPDH) and β-actin were used as reference genes. All samples were normalized by the geometric mean of the expression levels of reference genes, and fold changes of target genes (Table S.1, Supporting Information) were related to the control groups using the ΔΔCt method, where Ct is the crossing point of the reaction amplification curves determined by the Realplex 2.2 software (Eppendorf).

2.5.3. Histology

Samples were washed with PBS and fixed in 10% formalin (Thermo Fisher Scientific) for 30 min at RT. Then, samples were embedded in Histogel specimen processing gel (Thermo Fisher Scientific), dehydrated through graded ethanol solutions, and embedded in paraffin for further sectioning using a microtome (HM355S, Microm, Thermo Scientific). Sections of 10 μm thickness were prepared and stained with Masson's Trichrome and Alizarin Red. Sections were observed under a transmitted light microscope (Zeiss, Germany).

2.5.4. Immunostaining

Histology sections were also used for immunocytochemistry analysis of specific osteogenic markers. Firstly, sections were deparaffinised, and antigen retrieval was performed using citrate buffer (10 mM sodium citrate (Sigma-Aldrich), 0.05% Tween20 (Bio-Rad), pH 6). Thereafter, the sections were surrounded with a hydrophobic liquid barrier and permeabilised with 0.2% (v/v) Triton X-100 (Sigma-Aldrich) for 15 min at RT. Then, samples were rinsed with PBS and blocked with 3% (w/v) bovine serum albumin (BSA) in PBS for 30 min at RT. Later, samples were incubated with a primary antibody against osteopontin (OPN; rabbit anti-OPN antibody, 1:200, ab8448, Abcam, UK) or osteocalcin (OC, mouse anti-OC antibody, 8 μg/mL, MAB1419, R&D Systems, USA) in 1% (w/v) BSA in PBS, overnight at 4 °C. After removing the antibody solution, samples were washed 3 times with 0.05% Tween20-PBS for 15 min. Afterwards, samples were incubated with the corresponding secondary antibody labelled with AlexaFluor 488 (Donkey anti-rabbit IgG (H + L), 1:500, A21206, ThermoFisher Scientific), or AlexaFluor 488 (Donkey anti-mouse IgG (H + L), 1:500, A21202) for 1 h at RT, protected from light. Then, once the samples were washed with 0.05% Tween-PBS, nuclei, and cytoskeleton were stained with DAPI (1:1000 in PBS, Sigma-Aldrich) and phalloidin-TRITC (1:100 in PBS, Sigma-Aldrich), respectively, at RT for 1 h. After a final washing with 0.05% Tween20-PBS, samples were mounted with Vectashield fluorescence mounting medium and visualized using a transmitted and reflected light microscope with fluorescence (Axio Imager Z1m, Zeiss).

2.6. Effect on endothelial cells

2.6.1. Angiogenesis assay

Immortalized human umbilical vein endothelial cells (EA.hy926 cell line, CRL-2922, ATCC, USA) were expanded and cultured using complete DMEM – low glucose (Sigma-Aldrich) – supplemented with 10% FBS and 1% A/A – using the standard culture conditions.

Each cryogel scaffold was initially seeded with 1.5×10^5 hASCs and cultured for 3 days under complete α-MEM. Afterwards, 4.5×10^5 endothelial cells (EA.hy926 cells) were seeded on these scaffolds, resulting in a final ratio of 1:4 based on the initially seeded hASCs. Then, samples were cultured with complete α-MEM:D-MEM-Low Glucose (1:4 ratio) for 7 days, with medium replacement every other day. To evaluate the proangiogenic properties of the samples, they were processed as described in the above section and immunostained using a primary antibody anti CD31-APC conjugated (FAB3567A, R&D Systems, USA). Afterwards, nuclei and cytoskeleton were stained using DAPI and Phalloidin, as previously described. The samples were visualized using confocal laser scanning microscope (N = 3).

2.6.2. Migration assay

Cryogel scaffolds were incubated in 1 mL of α-MEM with 1% A/A solution (without FBS supplementation) at 37 °C. After 24 h of incubation, the supernatant was collected abs used as conditioning medium to perform the migration assay. For this, μ-Slides Chemotaxis chambers (Ibidi, Germany) were used following the manufacturer's instructions. First, 0.25×10^6 endothelial cells (EA-hy926 cells) in DMEM – low glucose with 1% A/A solution (without FBS supplementation) where loaded on one side of the chamber and allowed to adhere for 20 min. Afterwards, the conditioned media from each sample was loaded on the other side of the chamber. Thereafter, the chambers were incubated in an Incubation microscope (Zeiss, Germany), and the migration was recorded through time lapse on the same microscope for 24 h, as previously described (Chahal et al., 2021). For each group, 20 cells per chamber were randomly selected and cell tracking from two chambers per group was used to generate final tracking data (N = 40). Tracking data obtained from ImageJ were imported into the Chemotaxis and Migration tool (V2.0, Ibidi, Germany).

2.7. Statistical analysis

The statistical analysis was conducted with GraphPad Prism version 9.0 (GraphPad Software Inc., San Diego, USA) using one-way analyses of variance (ANOVA) followed by Tukey post hoc test, or a two-way ANOVA with Bonferroni post-test, to study the influence of two categorical independent variables. The values were considered different for a level of significance of $p < 0.05$. Statistically significant values are annotated in their respective graphs and the data is represented by mean ± standard deviation.

3. Results and discussion

3.1. Bioinspired mineralization of CNCs

In native bone, the precipitation of calcium and phosphate ions to form HAp is regulated by anionic NCPs, which are supposed to act as nucleation inhibitors by stabilizing its amorphous CaP precursors (Gorski, 2011; Yu & Wei, 2021). Nanocelluloses, including CNCs, have been considered as natural source-based nanoparticles for numerous high-performance applications in materials science, as templates for the production of relevant organic-inorganic hybrid nanocomposites or as nanofillers and crosslinking agents (Islam et al., 2018; Klemm et al.,

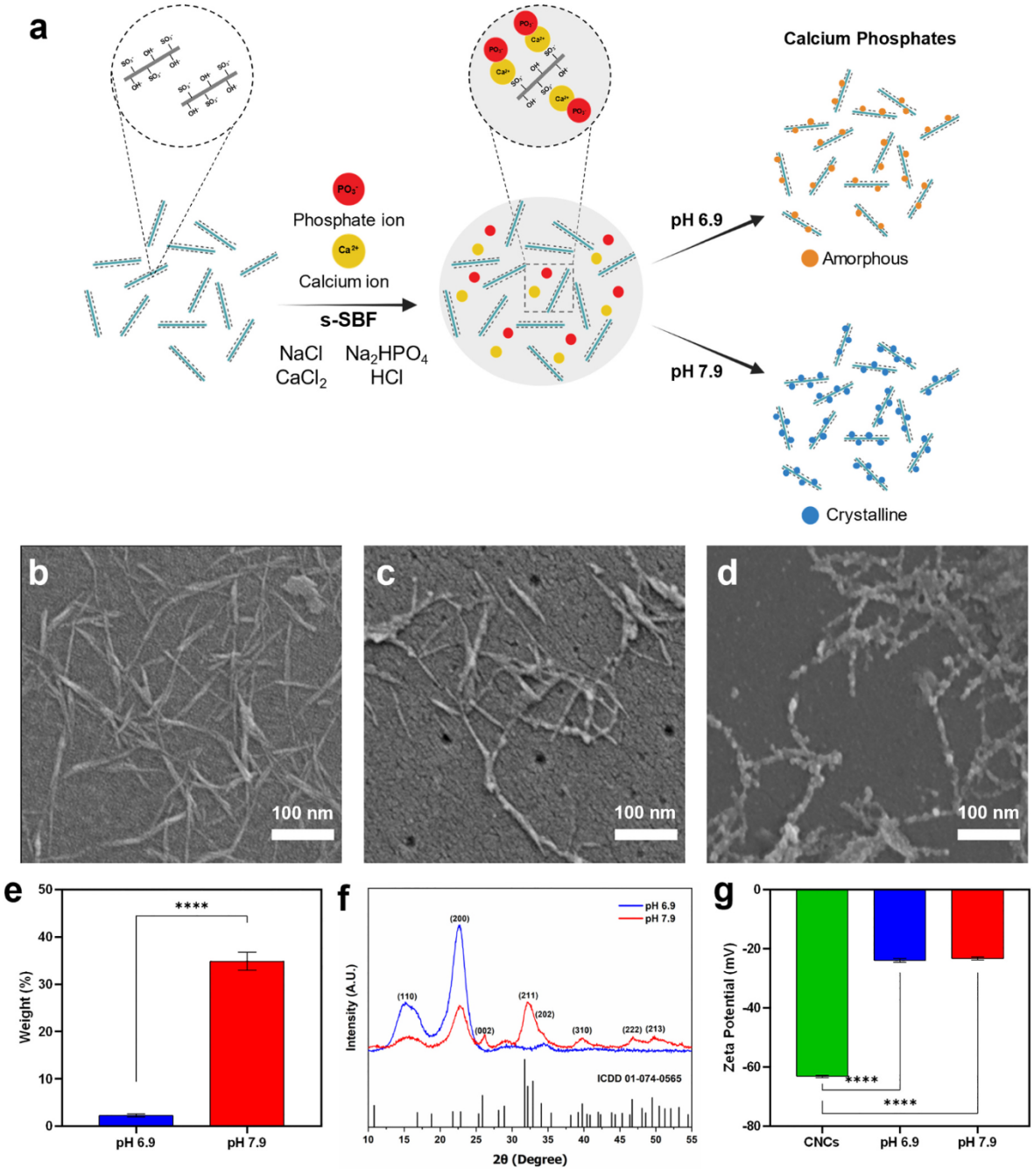


Fig. 1. Nanostructure, composition, and characterization of the biomineralized CNCs (m-CNCs). (a) Schematic of the biomineralization approach; SEM images of (b) non-mineralized CNCs, (c) m-CNCs (pH 6.9), and (d) m-CNCs (pH 7.9). Scale bar: 100 nm; (e) TGA analysis of the m-CNCs; (f) XRD analysis of m-CNCs produced at pH 6.9 and 7.9 and reference spectra of HAp (ICDD 01-074-0565). (g) Zeta potential of pristine CNCs and m-CNCs produced at pH 6.9 and 7.9. Statistical significance: ****$P < 0.0001$.

2018). Leveraging on these features and their surface chemistry, particularly the negatively charged character given by the SO_3^- groups, we pretended to mimic the role of anionic NCPs by inducing a biomineralization process on their surface to improve the biofunctionality of scaffolds for bone tissue engineering.

We produced CNCs by the typical sulfuric acid hydrolysis of microcrystalline cellulose derived from wood pulp (Bondeson, Mathew, & Oksman, 2006; Domingues et al., 2015). The produced CNCs exhibited the characteristic rod-shaped morphology with average length 200 nm and height of 4 nm (Fig. S1, Supporting Information) in agreement with previous works (Mendes, Gómez-Florit, Pires, et al., 2018; Silva et al., 2018). During its production, CNCs are simultaneously grafted with anionic sulfate half-ester groups on their surface, which results in 225 ± 10 mmol/kg of surface sulfate groups (-SO_3^-). These results agree with those reported for CNCs isolated from different cellulose sources by sulfuric acid hydrolysis that typically contain 80–350 mmol/kg of anionic sulfate half-esters introduced at some of the surface hydroxyl groups (Domingues et al., 2015; Foster et al., 2018).

Bioinspired by the role of anionic NCPs on the nanoscale mineralization process, we used negatively charged CNCs as template to control the growth of CaP on their surface and prevent their uncontrolled precipitation as crystalline HAp phases from supersaturated mineralization solutions (van Kemenade & de Bruyn, 1987). For this, we incubated CNCs with an s-SBF solution without Mg^{2+}, HCO_3^-, and SO_4^{2-} to effectively precipitate CaP on CNCs surface and prevent other undesired precipitation products, as calcium sulfates or calcium carbonates, or calcium (Ca^{2+}) substitution by other competitor cations as Mg^{2+}. During this process, calcium and phosphate ions from the supersaturated s-SBF are combined with the sulfate and hydroxyl groups on the surface of CNCs via hydrogen and ionic bonding (Fig. 1a), to form a stable mineralization site (Gebauer, Völkel, & Cölfen, 2008; Kumar et al., 2014; Si, Cui, Wang, Liu, & Liu, 2016). Consequently, variations of pH and [Ca^{2+}/SO_3^-] ratios alter the relative concentrations of the protonated forms of phosphate ions ($H_2PO_4^-$, pH < 7 or $HPO4^{2-}$ and PO_4^{3-}, pH > 7) and thus the chemical composition, the amount, and solubility of the CaP minerals that are being formed (Lynn & Bonfield, 2005; Wang & Nancollas, 2008). In this sense, it is crucial to establish the right balance between Ca^{2+}/SO_3^- and pH so CaP can be effectively deposited on the surface of CNCs rather than being spontaneously formed in the bulk solution, away from their surface. Therefore, we screened different mineral formation conditions, varying the pH of s-SBF solution (6.9 or 7.9) and the ratio between calcium ions [Ca^{2+}] and CNCs sulfate groups [–SO_3^-] (Ca^{2+}/SO_3^- molar ratio = 10, 20 or 40) (Fig. 1a).

Scanning electron microscopy (SEM) images of non-mineralized controls (Fig. 1b) showed visible morphological differences from mineralized samples obtained with a Ca^{2+}/SO_3^- ratio = 20 (Fig. 1c–d), pointing to the presence of mineral nanosized structures on CNCs' surface. Moreover, SEM images also showed that significant amounts of non-CNC bound inorganic nanoparticles were formed for the Ca^{2+}/SO_3^- ratio = 40 (Fig. S2, Supporting Information). In contrast, for the Ca^{2+}/SO_3^- ratio = 10, very few mineralized nanostructures were formed on the surface of CNCs compared to the other ratios (Fig. S2, Supporting Information). These results demonstrate that there is a balance between Ca^{2+} and SO_3^- concentration that favors the preferential nucleation and growth of CaP on the surface of CNC instead of its random occurrence in the s-SBF solution. As the [Ca^{2+}/SO_3^-] ratio raises from 10 to 40, the fraction of calcium and phosphate ions in the s-SBF solution that are not interacting with CNCs sulfate groups also increases (Huang et al., 2019; Ishikawa et al., 2015), leading to the formation of a higher fraction of mineral components that are not linked to the CNCs. On the other hand, when [Ca^{2+}/SO_3^-] ratio decreases, the number of mineral nanostructures seen on CNCs surface also decreases, being the lowest for the [Ca^{2+}/SO_3^-] ratio 10, where less calcium ions are proportionally available to interact with the excess of CNCs sulfate groups used under this condition and, thus, more CNCs remain unmodified. These results indicate that, from the tested condition, the [Ca^{2+}/SO_3^-] ratio of 20 is the ionic concentration that favors the mineral growth at the CNCs surface, in line with what was also previously suggested for calcium carbonate nanoparticles (Gebauer et al., 2011). Thus, Ca^{2+}/SO_3^- ratio = 20 was selected as condition for further analysis and later incorporation into the cryogel scaffolds.

Next, we tested the effect of pH on the quality of mineral components on CNC surface. We found that the pH of s-SBF solution influenced the formation and chemical nature of these mineral nanostructures (Fig. 1c–d and Fig. S2, Supporting Information). In basic conditions (pH 7.9), the mass fraction of nanosized structures was higher than in slightly acidic conditions (pH 6.9) (Fig. 1b–c). This can be explained by the presence of less protonated forms of phosphate ion (HPO_4^{2-} and PO_4^{3-}, pH > 7) that are more reactive with the calcium ions linked to the sulfate groups of CNCs, forming increased amounts of mineral nanostructures (Lynn & Bonfield, 2005; Wang & Nancollas, 2008). These results agree with the quantification of mineral content of the hybrid nanoparticles by thermogravimetric analysis, which was higher for particles produced at pH 7.9 than at pH 6.9 (Fig. 1e and fig. S3, Supporting Information).

Energy dispersive spectroscopy (EDS) profiling was used to determine the Ca/P ratio of the mineral nanostructures formed on the surface of m-CNCs. The CNCs mineralization protocol with a ratio (Ca^{2+}/SO_3^-) = 20 and at pH 6.9 and 7.9, showed Ca/P molar ratio of 1.85 and 1.7, respectively (Table S2, Supporting Information). These results are consistent with reported values for CaP, including the ratio of about 1.67 of HAp and native human bone, but also for other forms of amorphous CaP species, which show Ca/P ratios of 1.2–2.2 (Pina et al., 2015).

Next, we evaluated the crystallinity of the nanocomposites by X-ray diffraction analysis (XRD) (Fig. 1f) and calculated the crystallite size formed in each condition using the Scherrer's equation (Fig. S4, Supporting Information). The peaks at 2θ = 16° and 22.5° were assigned to the characteristic planes (110) and (200) of cellulose, respectively (Kumar et al., 2014; Si et al., 2016). After the mineralization protocol, the samples produced at pH 7.9 exhibited the known peaks of HAp at 2θ = 26.0° (002), 32.1° (211), 34.3° (202), 39.7° (310), 46.7° (222), and 49.7° (213) while the samples produced at pH 6.9 only showed a broad and diffuse peak at 34.3° (202) (Huang et al., 2019; Kumar et al., 2014). These results suggest that depending on the pH of the mineralization solution, CaP on m-CNCs exhibited different crystallinity. The mineralization protocol at pH 7.9 resulted in m-CNCs exhibiting characteristic and higher intensity peaks typical of hexagonal crystal form of HAp than the protocol at pH 6.9, which showed only minor and flatter HAp-associated XRD peaks. Moreover, the peaks corresponding to HAp of m-CNCs samples produced at pH 7.9 showed higher intensity than those corresponding to the crystalline cellulose, while for the samples produced at pH 6.9 the intensity of HAp-associated peaks were significantly lower than those of cellulose. These differences are also reflected on the calculated crystallite sizes of CaP formed on the m-CNCs, that were 11.8 ± 1.1 nm when produced at pH 7.9 (Fig. S4, Supporting Information), which are in the same range of HAp found in human bone (Londoño-Restrepo, Jeronimo-Cruz, Millán-Malo, Rivera-Muñoz, & Rodriguez-García, 2019), whereas for m-CNCs produced at pH 6.9 this parameter could not be calculated due to the lack of any well-defined peak, as expected from their poorly crystalline or more amorphous nature. Altogether, these results suggest that mineralization at pH 7.9 favors the formation of crystalline CaP that resembles HAp on the CNCs surface, while predominantly amorphous CaP are obtained at pH 6.9. However, we acknowledge that the exact chemical nature of both mineral components cannot be unequivocally defined based on these data.

We also determined the surface charge of the different nanoparticles produced (Fig. 1g). The results show that both amorphous (pH 6.9) and crystalline (pH 7.9) m-CNCs have a similar net negative surface (−24.0 ± 0.6 and − 23.3 ± 0.4 mV, respectively) but significantly less negative than pristine CNCs (−63.3 ± 0.3 mV). This reveals that CNCs surface charge provided by its sulfate groups is partially screened by the newly grown mineral phase, also contributing to confirm the occurrence of the

proposed surface modification. These results are specially interesting considering the role of NCPs not only as regulators of the sequestration of mineral ions, but also as key players in the formation of negatively charged complexes of mineral precursors that enter collagen through electrostatic attraction and promote the intrafibrillar collagen mineralization (Gorski, 2011). Overall, these results indicate that the bio-inspired mineralization protocol of CNCs results in the formation of CaP with amorphous and crystalline structures, depending on the pH of the precursor solution.

3.2. Organic-inorganic cryogel scaffolds production and physical characterization

Collagen is the main organic component of bone, which has frequently inspired bioengineers to produce different types of hydrogels and scaffolds for bone TERM applications (Ferreira, Gentile, Chiono, & Ciardelli, 2012; Reznikov et al., 2016). Nevertheless, the use of collagen has several shortcomings mainly related to its xenogenic origin, limited bioactivity and high contractibility and degradability in culture (Ferreira et al., 2012). Bioinspired by the role of platelets in tissues healing microenvironment, we have previously reported bioactive cryogel scaffolds consisting of PL mechanically reinforced and chemically crosslinked with a-CNCs (Mendes, Gómez-Florit, Araújo, et al., 2020). These scaffolds exhibited elasticity and an interconnected porous network, which might be relevant for their delivery in defect sites and application for different defects shapes as well as to allow cell growth. Interestingly, PL is normally obtained from expired platelet units, which revalorizes a highly available clinical waste material, and can be produced from autologous or pooled batches, making it a very versatile biomaterial (Mendes, Gómez-Florit, Pires, et al., 2018). Thus, we hypothesized that the incorporation of m-CNCs in these PL-based scaffolds would mimic the protein-mineral composite nature of bone ECM and, synergistically with the PL bioactive content, contribute to drive stem cells responses towards osteogenic phenotype.

Firstly, we tested the amount of m-CNCs that could be incorporated in the PL-based cryogel scaffolds without compromising their stability. For this, different proportions of a-CNCs (0–2.4 wt%, Fig. S5, Supporting Information) and m-CNCs (0–2.4 wt%) were mixed with PL (maintaining the total concentration of nanoparticles of 2.4 wt%). The cryogel scaffolds with an m-CNCs mass fraction higher than 75% of total nanoparticles showed limited structural integrity and underwent fast disintegration when immersed in PBS (Fig. S6, Supporting Information).

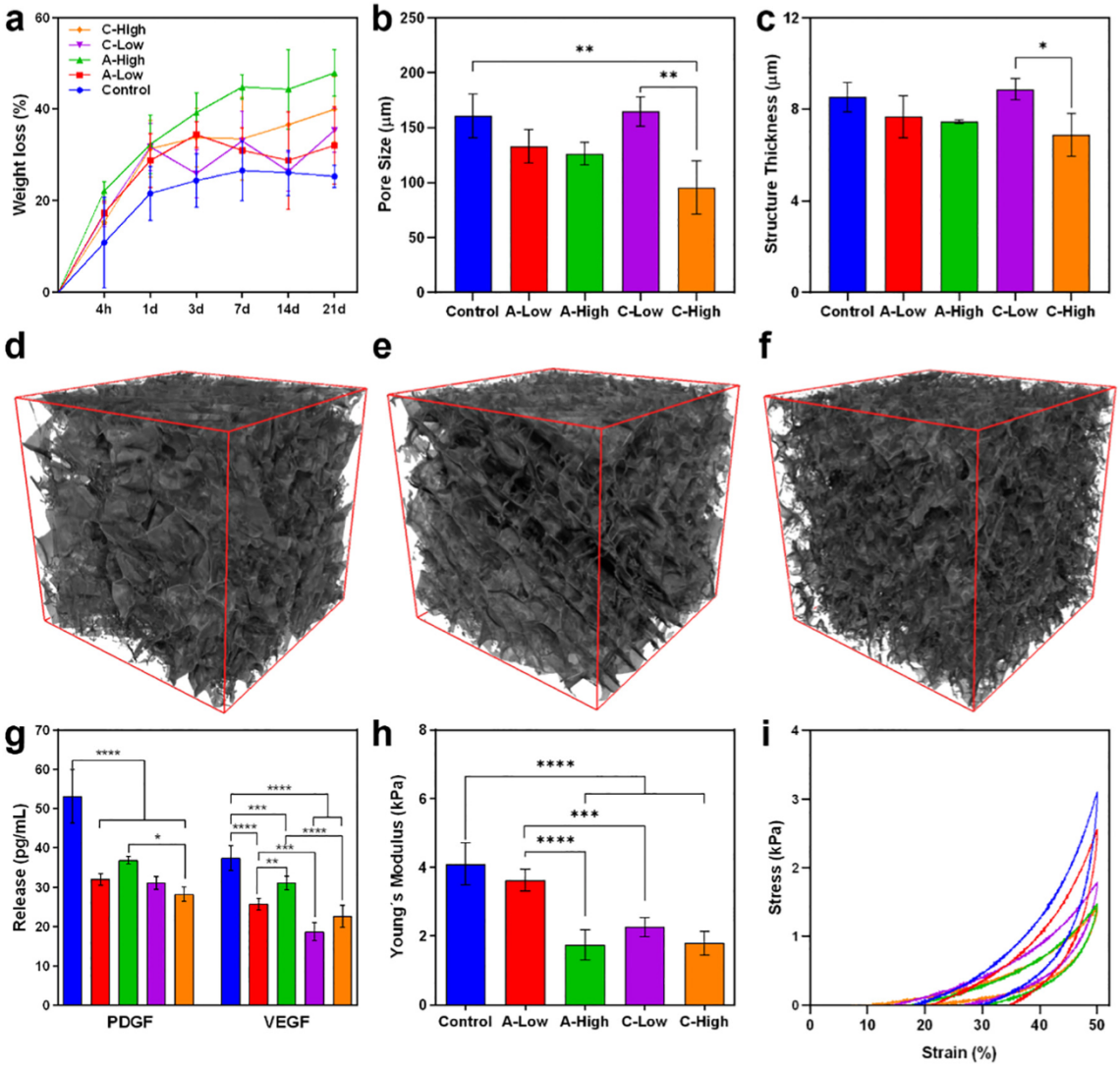


Fig. 2. Physical properties of the cryogel scaffolds. (a) Weight loss of the cryogel scaffolds over 21 days in PBS; (b) pore size and (c) structure thickness of the developed cryogel scaffolds and reconstructed images of the (d) control, (e) A-High, and (f) C-High formulations (4.5 μm^3) determined by µ-CT; (g) quantification of PDGF-BB and VEGF on the cryogel scaffolds releasates after 24 h in α-MEM without FBS; (h) Young's modulus from the uniaxial compression stress-strain curves; (i) stress-strain curves of a loading and unloading cycle of each sample up to $\varepsilon = 50\%$. Statistical significance: $^{*}P < 0.05$, $^{**}P < 0.01$, $^{***}P < 0.001$, and $^{****}P < 0.0001$.

On the other hand, all the other tested mineralized formulations (50% and 25% of m-CNCs, named High and Low, respectively) maintained their structure and showed a high mold fidelity, comparable to the non-mineralized cryogel scaffolds (Fig. S6, Supporting Information). From these findings we could infer that the presence of a-CNCs is crucial for the structural integrity of the cryogel scaffolds due to the chemical covalent crosslinking between a-CNCs and the amine groups of PL proteins through reversible Schiff base bonds (Dash, Foston, & Ragauskas, 2013; Mendes, Gómez-Florit, Pires, et al., 2018).

We further characterized the structural integrity of our mineralized cryogel scaffolds by measuring the weight loss of the samples immersed in PBS for 21 days (Fig. 2a). All formulations eroded and lost weight over time, though cryogel scaffolds with high mass fractions of both types of m-CNCs showed relatively higher weight loss (47.9 ± 4.4% and 39.9 ± 6.1%, respectively) in comparison with the formulations containing low contents of m-CNCs (32.1 ± 7.3% for A-Low and 35.4 ± 4.2% for C-Low) and the control group (25.3 ± 2.0%). In summary, as anticipated during the initial testing, although the formulations with high and low m-CNCs content might decrease the crosslinking degree between the a-CNCs and amine groups of PL-derived proteins, the initial and long-term structural integrity of the mineralized cryogel scaffolds was maintained.

Moreover, the water uptake ability of the cryogel scaffolds was evaluated (Fig. S7a, Supporting Information). In general, the addition of m-CNCs did not markedly affect the high water absorption potential of the cryogels, although a more significant reduction was detected for the High m-CNC content conditions, probably due to de impact that these nanoparticles have over the materials microstructure. In order to study the cryogel scaffolds at microstructural level, we used micro-computed tomography (μ-CT) (Fig. 2b, c and Table S2). All groups exhibited a similar open microporosity (94–95%, Table S2), which is ~4–20% higher than the porosity previously reported for different scaffolds for bone tissue engineering (Carlström et al., 2020; Huang et al., 2019; Kumar et al., 2014; Torgbo & Sukyai, 2019), and is critical for cell functions and nutrient diffusion and metabolic waste removal (Murphy, O'Brien, Little, and Schindeler, 2013; Zhang, Lu, Kawazoe, & Chen, 2014). Nevertheless, we could observe that mineralized cryogel scaffolds showed decreased pore size and wall thickness compared to the control group, which was significantly different on the C-High formulation (Fig. 2b, c). These results might be related to the lower mass fraction of a-CNCs in the mineralized samples, which induced a lower degree of crosslinking of the cryogels. We hypothesize that this lower crosslinking might be more permissive to ice crystals growth during cryogelation and, at the same time, lead to a higher compaction of the nanoparticles on the pore walls, decreasing their thickness. Furthermore, these findings corroborated the previous water absorption results since the diminishment of the absorption ability of the cryogel scaffolds might be a result of the decrease of both the pore size and structure thickness. Overall, these results indicate that the amount of a-CNCs determines in a greater extend the physical properties of our cryogel scaffolds.

The release of PL-derived bioactive molecules from the developed cryogel scaffolds was evaluated using immune-based protein quantification (Fig. 2g and Supporting information). As representative components of interest, we selected PDGF and VEGF, a chemotactic and a proangiogenic GF, respectively, that are known to play pivotal roles in boosting the cells' mitogenic activity and supporting endothelial sprouting, which are crucial in bone healing and regeneration (Koons et al., 2020). Contrarily to what would be expected from samples with higher weight loss, the immunodetection assay showed a decreased release of both GFs in mineralized groups compared to the control (Fig. 2g). The more effective entrapment of these GFs in the cryogel scaffolds might result of either the microstructural alterations observed in the material or a favored interaction of these biomolecules with the mineral components. These effects might be compared to the role of native ECMs on the sequestration and regulation of GFs presentation in tissue microenvironments, which has been proven to increase GFs half-lives and localized action (Teixeira et al., 2020), and thus possibly contribute to prolong the bioactivity of the proposed mineralized cryogel scaffolds.

One of the main limitations typically associated to cryogels is their low mechanical strength mainly due to their open microporous structure [57]–[59]. The highly stiff CNCs have been applied as reinforcement nanofillers of these type of soft matrices (Domingues et al., 2014; Foster et al., 2018), including our PL-based systems, enhancing their mechanical properties and biologic performance (Chahal et al., 2021; Mendes, Gómez-Florit, Araújo, et al., 2020; Mendes, Gómez-Florit, Pires, et al., 2018; Silva et al., 2018). To determine the impact of m-CNCs incorporation on the mechanical properties of the cryogel scaffolds, uniaxial compression tests were performed under hydrated conditions (Fig. 2h, i and Fig. S7b–f). In general, all the mineralized formulations showed lower Young's moduli (between 1.7 ± 0.4 kPa for A-High and 3.4 ± 0.3 kPa for A-Low) than the control group (4.1 ± 0.6 kPa). As would be expected, the higher mass fraction of a-CNCs in control samples results in increased crosslinking density, leading to stiffer cryogel scaffolds compared to the mineralized formulations, which have lower degrees of covalent crosslinking. A similar effect was also noticeable for the m-CNCs mass fraction, with the Low formulations showing increased elastic modulus compared to High formulations, although it was only significant for amorphous samples. These values are obviously lower than the reported Young's modulus of trabecular and cortical bone (in the GPa order (Rho, Ashman, & Turner, 1993)), making our scaffolds more suitable for applications in non-load bearing mineralized tissues (e.g. in some maxillofacial injuries or dental extraction sockets) or as bioactive bone fillers to promote a faster regeneration of non-healing fixated bone defects. Furthermore, to test the injectability and shape recovery capacity of the developed formulations, the cryogels were subjected to compression cycles (Fig. 2i). All formulations could be compressed up to 75% strain without being structurally or mechanically compromised (Movie S1, Supporting Information). Upon relaxation, cryogel scaffolds elastically recovered their original shape, displaying a fast deformation reversion (on the order of seconds, see Movie S1, Supporting Information). Moreover, upon three additional compression-relaxation cycles, an overlap of the cyclic stress−strain curves with similar elastic modulus values was observed (Fig. S7b–f, Supporting Information). These results demonstrated that mineralized cryogel scaffolds maintain their mechanical strength and high compression resilience under continuous and dynamic compression while withstanding extensive deformations without being destroyed, despite the decrease of the Young's modulus with the addition of the m-CNCs. Moreover, these results also indicate that the developed mineralized cryogel scaffolds present remarkable elastic properties that allow them to be compressed and delivered in bone defects (e.g. to promote bone regeneration in tooth extraction sockets or in tumor-related defects, see Fig. S8, Supporting Information). In previous works, CaP-polymer composites were used to produce different scaffolds, which showed high stiffness and elasticity, required for bone grafts, although their bioactivity was limited (Huang et al., 2019; Jakus et al., 2016; Kumar et al., 2014). Here, our mineralized cryogel scaffolds showed high elasticity and, at the same time, high bioactivity steaming from the PL biomolecules such as growth factors, which might represent an advantage to promote bone regeneration.

3.3. Biomimetic mineralization stimulates osteogenic commitment

In the study of cellular responses to the cryogel scaffolds, we first evaluated whether the incorporation of m-CNCs could affect the cytocompatibility of PL-based biomaterials. For this, the viability of human adipose-derived stem cells (hASCs) seeded onto the cryogels was evaluated by live/dead assay (Fig. 3a–e). Three days after seeding, results showed a high cell viability (>90%) for all formulations without significant differences among them (Fig. 3f). Moreover, hASCs displayed a spindle-shape morphology and were distributed over the entire cryogel

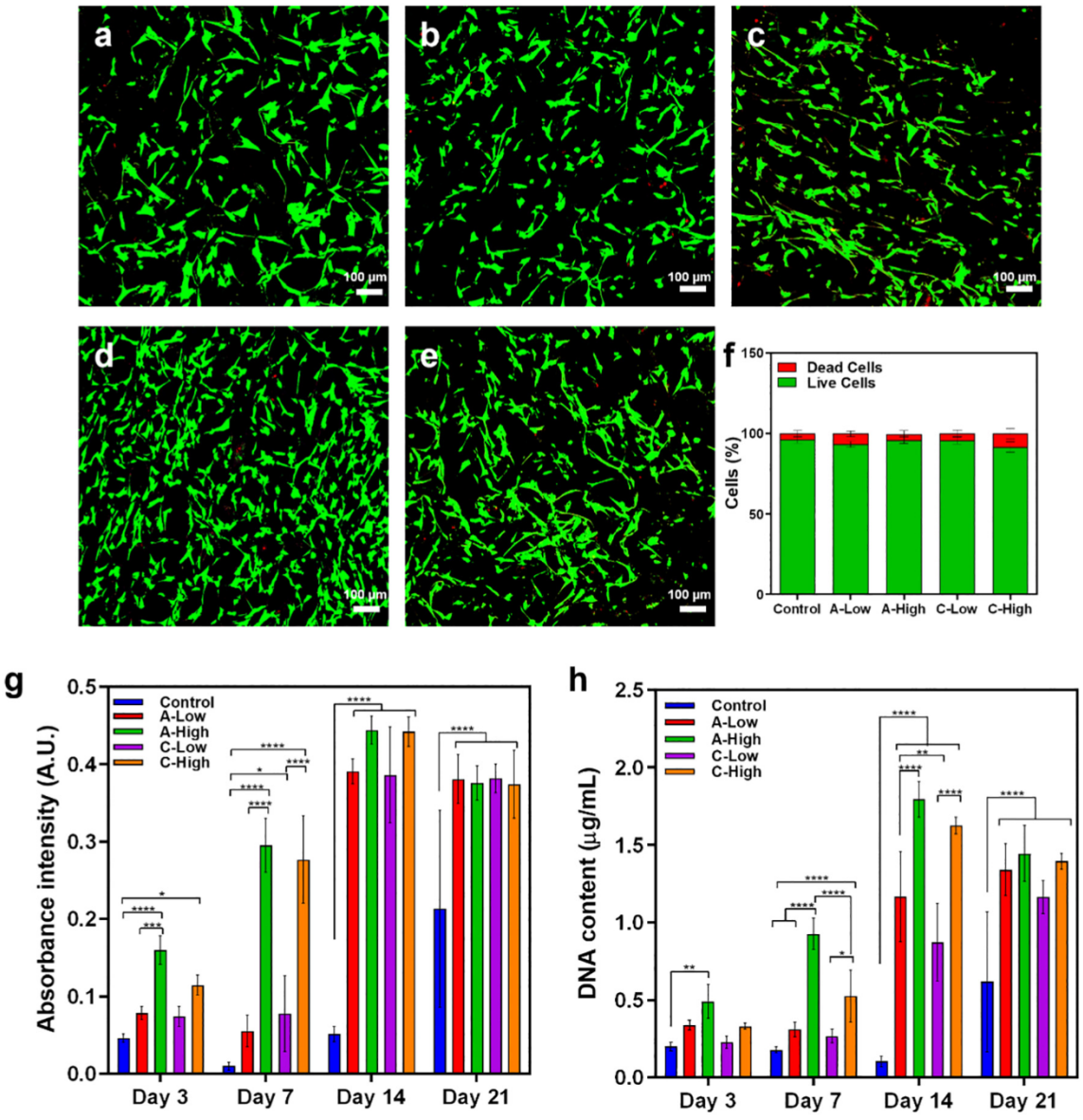


Fig. 3. In vitro evaluation of the cytocompatibility of the cryogel scaffolds. Representative images after live/dead staining (green: live cells; red: dead cells) of hASCs seeded on cryogel scaffolds after 3 days in culture: (a) control, (b) A-Low, (c) A-High, (d) C-Low, and (e) C-High. Scale bar: 100 µm; (f) respective cell viability quantification. All groups showed more than 90% cell viability after 3 days of culture; (g) metabolic activity and (h) DNA content of hASCs seeded on the scaffolds. Statistical significance: $^{*}P < 0.05$, $^{**}P < 0.01$, $^{***}P < 0.001$, and $^{****}P < 0.0001$.

scaffold network, likely due to their high open porosity and presence of cell-adhesive proteins from PL (e.g. fibrinogen, fibronectin, vitronectin) (Fekete et al., 2012; Mendes, Gómez-Florit, Osório, et al., 2020) that support hASCs attachment. This represents an advantage of our scaffolds compared with other scaffolds prepared from rather bioinert polymers, which do not possess cell-binding sites (Huang et al., 2019; Kumar et al., 2014). Furthermore, since we used low amounts of m-CNCs and a-CNCs (only up to 2.4 wt%) to produce the scaffolds, no cytotoxic effects were detected. Thus, these results demonstrate that the designed nanocomposite scaffolds are not cytotoxic and can support cell growth, as expected since, in general, all nanocelluloses are considered biocompatible materials (Khan et al., 2021).

We then evaluated if the mineralized cryogel scaffolds could influence viability and the proliferation of hASCs. For that, the metabolic activity (Fig. 3g) and cell proliferation measured by DNA quantification were evaluated over cell culture time (Fig. 3h). All formulations containing m-CNCs nanoparticles presented higher metabolic activity and cell proliferation than the control scaffolds at each time point. Moreover, no significant differences in these parameters were observed between formulations containing the same amount of amorphous and crystalline m-CNCs. Nevertheless, A-High and C-High formulations presented increased metabolic activity and cell proliferation compared to A-Low and C-Low, respectively, until day 14 of culture. After 21 days, although the values for both indicators are comparable for all mineralized groups, DNA content increased in A-Low and C-Low formulations, while it decreased in A-High and C-High formulations compared to the previous time point, which can be potentially related to onset of hASCs lineage commitment, or with the reduction of proliferation due to increased cell-cell contact (Thrivikraman et al., 2019). In addition, A-High condition presented a higher value of metabolic activity and DNA content than C-High, which can be possibly justified by the faster passive solubilization of amorphous CaP minerals (Hoppe, Güldal, & Boccaccini, 2011; Maeno et al., 2005). This leads to an increased concentration of extracellular calcium and phosphate ions, which has been shown to promote osteoblasts proliferation, differentiation, and ECM mineralization by directly activating intracellular mechanisms that influence Ca-sensing receptors

in osteoblastic cells (Hoppe et al., 2011; Maeno et al., 2005; Marie, 2010).

It is well known that cells sense and respond to the biochemical and biophysical properties of the extracellular microenvironment in which they are embedded (Hsieh et al., 2016; Lutolf, Gilbert, & Blau, 2009). To evaluate the potential osteogenic effects resulting from the incorporation of m-CNCs into the scaffolds, the cell-seeded constructs were cultured under basal media conditions (without the aid of any osteogenic supplement). The expression and activity of alkaline phosphatase (ALP), a hallmark of functional bone, were used to determine the potential of the scaffolds to promote osteogenic differentiation of hASCs. Scaffold formulations including m-CNCs showed higher early *ALP* gene expression (Fig. S9a, Supporting Information) and higher ALP activity than the control group at all time points (Fig. 4a). Moreover, ALP activity increased faster and reached higher levels on A-High and C-High formulations than on their respective Low conditions. Interestingly, we also observed that A-High ALP activity peaks at day 7, progressively decreasing until the end of culture time, while the other mineralized formulations reach their maximum ALP activity at day 14. Since ALP is an early osteogenic differentiation marker, this demonstrates that the number of m-CNCs nanoparticles, particularly the amount of CaP present, influences the rate of cells commitment towards the osteogenic lineage. Considering that the precursors of the intrafibrillar HAp are amorphous CaP (ACPs) sequestered by NCPs, such as osteopontin, which inhibit the nucleation of HAp and consequently the extrafibrillar deposition of HAp, formulations containing amorphous m-CNCs are the ones that better resemble the microenvironment of the natural bone nanoscale biomineralization (Gorski, 2011). In addition, the presence of amorphous CaP on the surface on CNCs as well as the negative charge presented by m-CNCs, besides mimicking the ACPs and the role of NCPs in native bone, respectively, can potentially act itself as an osteogenic supplement (Hoppe et al., 2011; Viti et al., 2016), inducing the osteogenic differentiation of seeded stem cells.

Furthermore, the transcription levels of genes associated with either osteoblastic/pre-osteocytic differentiation or bone metabolism and remodeling were also evaluated (Fig. 4b–f). The expression of *RUNX2*, a transcription factor involved in early osteogenic lineage commitment (Komori, 2009), was significantly up-regulated on both A-High and C-High formulations, compared to control group (Fig. 4b). Moreover, the expression of *COL1A1*, a downstream *RUNX2* target and the major protein of bone ECM (Komori, 2009), was also increased on mineralized groups at early time points, compared to the control. Another protein involved in the osteogenic differentiation process and bone metabolism and homeostasis is *BMP-2*, as a potent osteoinductive agent (Yamaguchi et al., 1991). We observed that after 14 days of culture, *BMP-2* expression was upregulated on all mineralized conditions, especially on samples with High m-CNCs content. Moreover, the expression of Dickkopf-related protein 1 (*DKK-1*), an osteoblasts maturation inhibitor (Lian, Gravallese, & Stein, 2011; Terpos & Gavriatopoulou, 2019), was downregulated on all mineralized conditions, possibly pointing to an early stage of hASCs osteoblastic commitment. Another interesting marker associated to osteoblasts maturation is podoplanin (*PDPN*), which is expressed by osteoblasts and immature osteocytes during their differentiation (Wehmeyer et al., 2019). We could observe that, by day 7, *PDPN* was highly expressed in all mineralized conditions compared to the control, except for the C-High formulation, while, by day 14, only A-High and C-Low still showed a high expression of this marker. Additionally, osteoprotegerin (*OPG*) expression, a key bone remodeling cytokine receptor that inhibits the osteoclastogenesis (bone resorption) (Terpos & Gavriatopoulou, 2019), showed a decreased expression by day 14 (Fig. S9b, Supporting Information). Furthermore, the expression levels of osteocalcin (*OC*), a late-stage marker for osteoblastic differentiation, were only noticeable after 14 days of culture (Fig. S9c, Supporting Information). These results suggest that hASCs commit into an osteoblast-like phenotype in contact with the biomimetic mineralization microenvironment provided by m-CNCs, particularly in A-High and C-High formulations, pointing to a high osteoinductive potential of the developed mineralized cryogels.

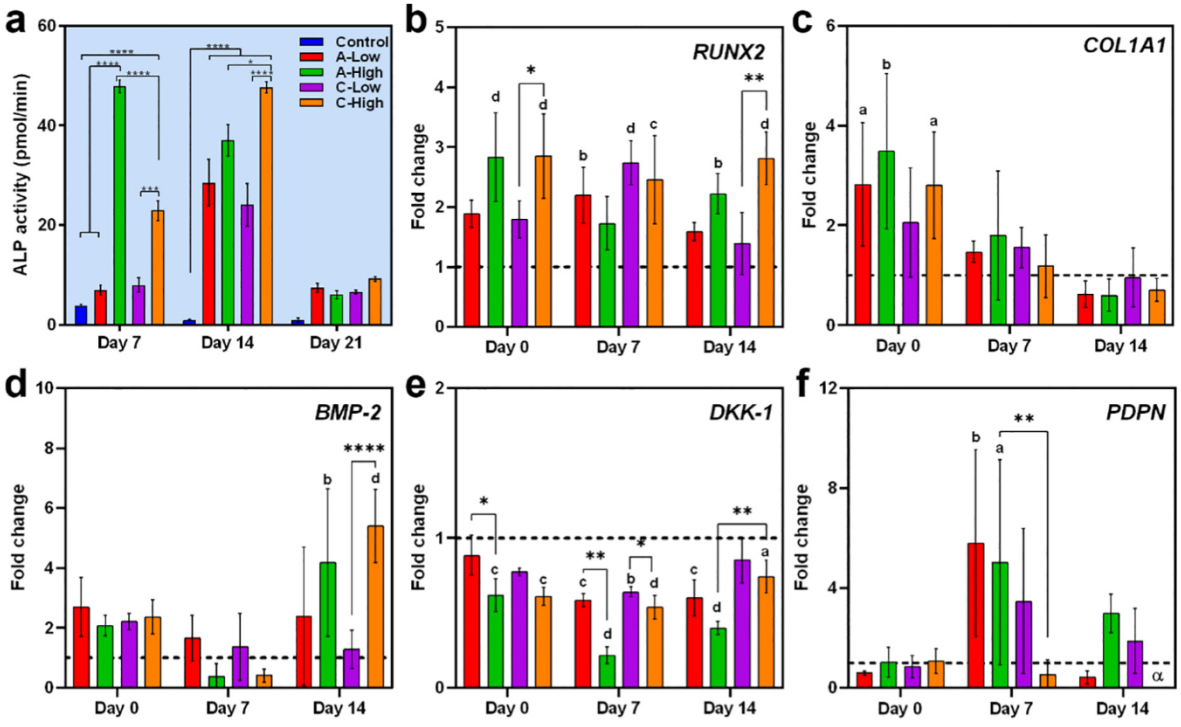


Fig. 4. In vitro evaluation of the ALP activity and gene expression of hASCs in the cryogel scaffolds. (a) ALP activity of hASCs seeded on the scaffolds. Gene expression of (b) RUNX2, (c) COL1A1, (d) BMP-2, (e) DKK-1, and (f) PDPN of hASCs seeded on the cryogel scaffolds for different times. Data is represented as fold changes respect to control group at each time point. Statistical significance: $^{a,*}P < 0.05$, $^{b,**}P < 0.01$, $^{c,***}P < 0.001$, and $^{d,****}P < 0.0001$, with a-d statistical differences with the control. (α) No expression was detected.

To further validate the gene expression results, we immunostained cells for osteopontin (OPN) and OC, two key late osteoblastic markers, after 21 days of culture (Fig. 5a–j). We could observe that cells were able to invade the cryogel scaffolds in all formulations. Consistent with our gene expression analysis, the number of cells positively stained for these markers was higher in High groups than in the respective Low homologues. Nonetheless, we could not observe major differences in the expression of these markers when comparing the mineralized groups with the control. Moreover, we used Alizarin Red staining as indicator of calcium deposition (Fig. 5k–o). It was observed that both A-High and C-High conditions presented increased mineralization compared to Low formulations and control, which showed only residual or superficial staining. These results indicate that although all formulations (mineralized and control) possess, to some extent, the ability to promote the expression of osteogenic differentiation markers in hASCs, effective ECM mineralization only occurred in High m-CNCs content formulations. In native bone, osteoblasts transition from a spindle-shape to a star-shape morphology as the surrounding matrix is transformed from a soft osteoid to a more mineralized matrix (Bonewald, 2011). In order to evaluate effects over hASCs morphology and ECM deposition, specimens were processed for trichrome staining (Fig. 5p–t). We could observe that reticular connective tissue (in light blue, between cells), associated to collagen deposition, was produced by hASCs in all scaffold formulations. Interestingly, A-High formulation (Fig. 5r) also showed more cells with an osteocyte-like phenotype (star shape, red arrows) with several cellular projections between them than the other formulations.

In summary, both A-High and C-High scaffold formulations induced an enhanced expression of osteogenic-related markers in hASCs. Nonetheless, among these, A-High showed a higher and earlier expression of osteogenic differentiation makers and ALP activity, the hallmark of mineralizing bone, and a lower expression of differentiation inhibitors. We hypothesize that A-High formulation emulates better the nanoscale biomineralization microenvironment and process, since in native mineralized tissues, ACPs are first deposited to be later matured into HAp crystals (Gorski, 2011). Moreover, the faster solubilization of the amorphous CaP and respective release of calcium ions, has been show to improve the osteoinductive properties of biomaterials (Hoppe et al., 2011). Collectively these results indicate that the type (amorphous vs crystalline) and amount of m-CNCs modulates the expression of osteogenic-related markers as well as the osteoinductive properties of the nanocomposite cryogel scaffolds.

3.4. Proangiogenic properties unaffected by mineralization

The vascularization of bioengineered scaffolds is a critical and challenging goal not only for a highly vascularized tissue such as bone but also for the TERM field (Bae et al., 2012). It maintains the vitality of the newly forming tissue by providing the nutrients, including oxygen, the removal of the metabolic waste products, and assure the immune response against foreign invasions. In this sense, to prove that our biomimetic strategy not only promotes the osteogenic commitment of cells but also supports angiogenesis, we co-cultured hASCs with endothelial cells and evaluated the expression of CD31, an endothelial marker (Fig. 6a–j). After 7 days of culture, cells on all cryogel scaffolds formulations expressed CD31 (Fig. 6a–e), which demonstrates that the incorporation of the m-CNCs did not negatively influence the proangiogenic properties of our cryogel scaffolds. Moreover, the High m-CNCs content constructs (Fig. 6h, j) showed more CD31 expression than the Low

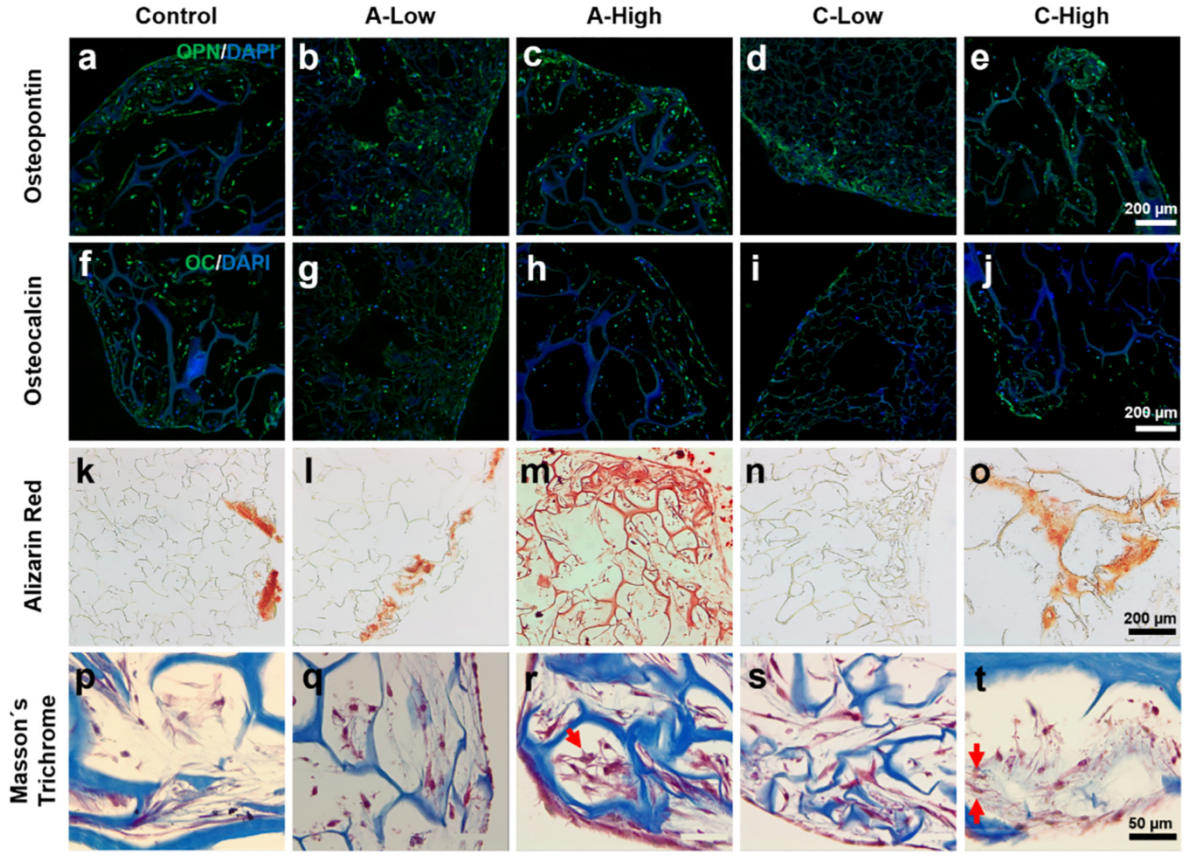


Fig. 5. Evaluation of the osteogenic commitment of hASCs seeded on the cryogel scaffolds. Representative immunocytochemistry images of the OPN (a–e) and OC (f–j) staining of the cryogel scaffolds seeded with hASCs after 21 days of culture (blue: nuclei; green: OPN or OC). Representative images of Alizarin Red (k–o) and Masson's Trichrome (p–t) staining of the developed cryogel scaffolds, seeded with hASCs, after 21 days of culture. Some cells present an osteocyte-like phenotype (red arrows). Scale bar: 200 µm (a–o) and 50 µm (p–t).

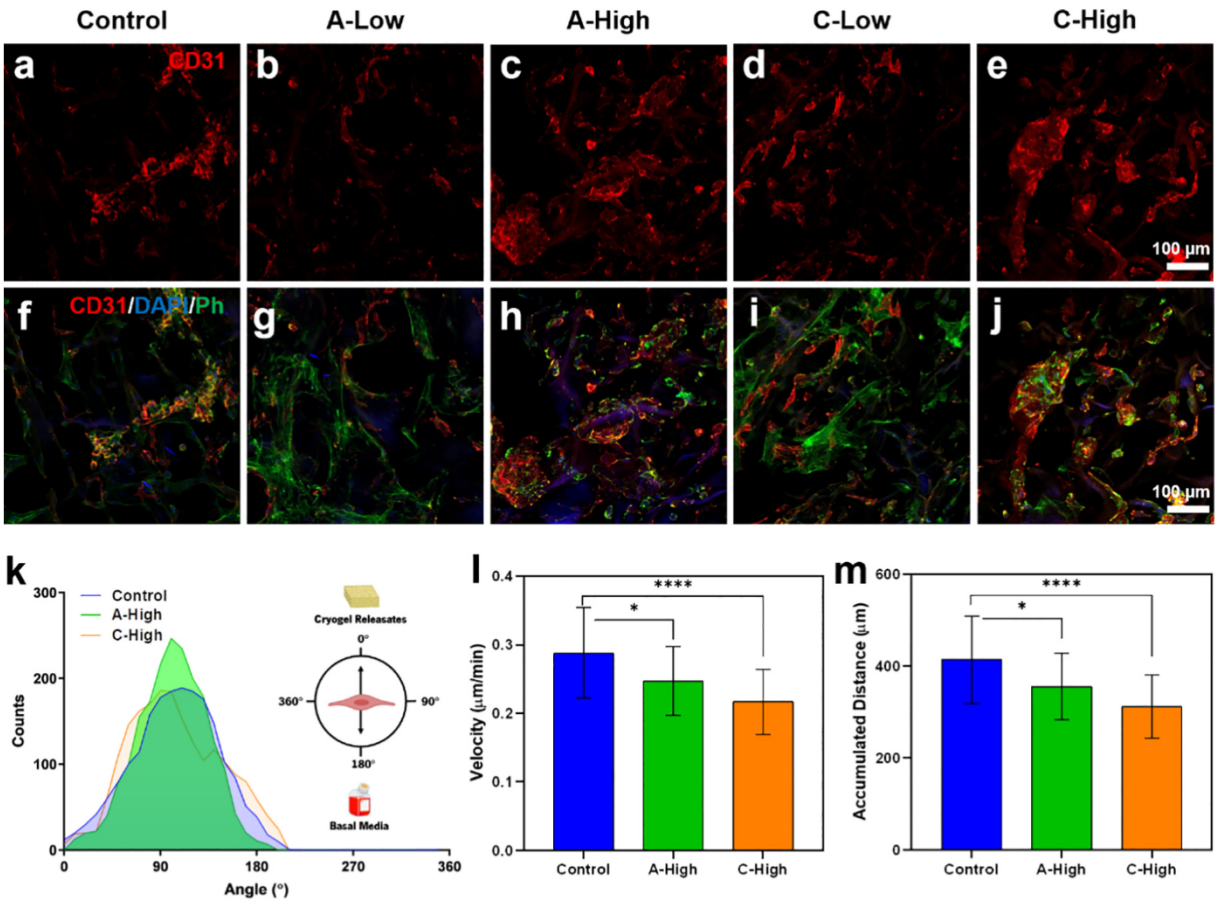


Fig. 6. In vitro proangiogenic and chemotactic behavior of the cryogel scaffolds. Representative immunocytochemistry images of the (a–j) CD31 staining of the cryogel scaffolds seeded with hASCs and endothelial cells after 7 days of culture (blue: nuclei; red: CD31; green: cytoskeleton). Scale bar: 100 µm. (k) Directionality, (l) velocity, and (m) accumulated distance of the migrating endothelial cells in the presence of High m-CNCs content cryogel scaffolds releasates. Statistical significance: $^{*}P < 0.05$, and $^{****}P < 0.0001$.

content conditions (Fig. 6g, i), which indicates that more cell junctions were formed, typical of endothelial structures.

Furthermore, to confirm this proangiogenic feature and to evaluate the potential of our constructs as powerful chemotactic agents for endothelial cells, we studied the migration of the endothelial cells on the presence of the releasates of the control and High m-CNCs content formulations. From the migration assay we could infer that the incorporation of m-CNCs did not affect the direction of endothelial cells' migration (towards the scaffolds releasates, Fig. 6k), but significantly decreased their migration velocity (Fig. 6l) and accumulated distance (Fig. 6m). These results might be correlated with the observed slower release of chemotactic and pro-angiogenic growth factors such as PDGF and VEGF from the mineralized scaffolds (Fig. 2b). We hypothesize that the slower release of these growth factors from the mineralized samples is responsible for the decreased endothelial cells migration in this assay, but their higher sequestration within the mineralized scaffolds might contribute for the observed increased CD31-positive endothelial structures. These results demonstrate that our mineralized cryogel maintain the high chemotactic and proangiogenic potential of its PL-CNC precursors, and are in line with previous works which have shown that PL-laden hydrogels promote chemotaxis of hASCs (Chahal et al., 2021) and the formation of neovascular structures (Silva et al., 2018; Zhang et al., 2021). In summary, together with their biomineralization and osteogenic potential, these angiogenic and chemotactic properties demonstrate the multifunctional character of our mineralized cryogel scaffolds to promote the regeneration of mineralized and vascularized tissues. Nevertheless, future in vivo studies will contribute to validate these results.

4. Conclusions

By combining PL as source of structural and bioactive cues with a-CNCs and m-CNCs as crosslinkers and mineralized nanofillers, herein we developed a bioinspired multifunctional scaffold that emulates the natural nanoscale biomineralization microenvironments. The selection of the production process parameters, namely Ca^{2+}/SO_3^{-} ratio = 20, allowed the production of mineralized hybrid nanoparticles. Moreover, controlling the pH of the mineralization protocol allowed to develop CaP with different chemical and physical nature. While the mineralization protocol at pH 6.9 resulted in m-CNCs with more amorphous CaP, the protocol at pH 7.9 resulted in m-CNCs with more crystalline CaP. We found that the developed mineralized cryogel scaffolds enhanced the metabolic activity, cell proliferation, and ALP activity of hASCs, in a dose-response fashion. Moreover, they also up-regulated the expression of bone-related markers, as *RUNX2*, *BMP-2*, and *COL1A1* in hASCs, which indicated a preferential stem cells differentiation towards osteogenic lineages. Among the different m-CNCs, those decorated with amorphous CaP induced the highest osteogenic response, probably because they mimic the natural biomineralization process through the solubilization of osteoinductive of calcium ions. Furthermore, we found that the mineralized scaffolds maintained the proangiogenic and chemotactic properties of their precursors. Overall, results suggest that m-CNCs, particularly the High-content amorphous condition, conferred to the developed scaffolds increased osteoinductive potential without negatively affecting their elasticity and PL-derived bioactivity, which might collectively be useful for applications targeting the regeneration of mineralized tissues.

Supplementary data to this article can be found online at https://doi.org/10.1016/j.carbpol.2022.119638.

CRediT authorship contribution statement

João P. Ribeiro: Investigation, Formal analysis, Visualization, Writing – original draft. **Rui M.A. Domingues:** Conceptualization, Investigation, Formal analysis, Validation, Methodology, Writing – review & editing. **Pedro S. Babo:** Methodology. **Liebert P. Nogueira:** Investigation, Formal analysis. **Janne E. Reseland:** Funding acquisition, Project administration, Resources. **Rui L. Reis:** Funding acquisition, Resources. **Manuel Gomez-Florit:** Conceptualization, Investigation, Formal analysis, Funding acquisition, Methodology, Project administration, Supervision, Validation, Visualization, Writing – review & editing. **Manuela E. Gomes:** Conceptualization, Funding acquisition, Project administration, Resources, Supervision, Writing – review & editing.

Declaration of competing interest

None.

Acknowledgements

We acknowledge the financial support from Research Council of Norway for project no. 287953 and from Portuguese Foundation for Science and Technology (FCT) for CEECIND/01375/2017 to MGF and 2020.03410.CEECIND to RMAD. We also acknowledge Dr. Margarida Miranda (3B's Research Group, University of Minho) for the TGA analysis.

References

Babo, P. S., Santo, V. E., Gomes, M. E., & Reis, R. L. (2016). Development of an injectable calcium phosphate/hyaluronic acid microparticles system for platelet lysate sustained delivery aiming bone regeneration. *Macromolecular Bioscience, 16*(11), 1662–1677. https://doi.org/10.1002/mabi.201600141

Bae, H., Puranik, A. S., Gauvin, R., Edalat, F., Carrillo-Conde, B., Peppas, N. A., & Khademhosseini, A. (2012). Building vascular networks. *Science Translational Medicine, 4*(160). https://doi.org/10.1126/SCITRANSLMED.3003688

Bharadwaz, A., & Jayasuriya, A. C. (2020). Recent trends in the application of widely used natural and synthetic polymer nanocomposites in bone tissue regeneration. *Materials Science and Engineering: C, 110*, Article 110698. https://doi.org/10.1016/j.msec.2020.110698

Bishnoi, A., Kumar, S., & Joshi, N. (2017). Wide-angle X-ray diffraction (WXRD). In *Microscopy methods in nanomaterials characterization* (pp. 313–337). Elsevier. https://doi.org/10.1016/B978-0-323-46141-2.00009-2.

Bjørnøy, S. H., Bassett, D. C., Ucar, S., Strand, B. L., Andreassen, J.-P., & Sikorski, P. (2016). A correlative spatiotemporal microscale study of calcium phosphate formation and transformation within an alginate hydrogel matrix. *Acta Biomaterialia, 44*, 254–266. https://doi.org/10.1016/j.actbio.2016.08.041

Bondeson, D., Mathew, A., & Oksman, K. (2006). Optimization of the isolation of nanocrystals from microcrystalline cellulose by acid hydrolysis. *Cellulose, 13*(2), 171–180. https://doi.org/10.1007/s10570-006-9061-4

Bonewald, L. F. (2011). The amazing osteocyte. *Journal of Bone and Mineral Research, 26*(2), 229–238. https://doi.org/10.1002/JBMR.320

Carlström, I. E., Rashad, A., Campodoni, E., Sandri, M., Syverud, K., Bolstad, A. I., & Mustafa, K. (2020). Cross-linked gelatin-nanocellulose scaffolds for bone tissue engineering. *Materials Letters, 264*, Article 127326. https://doi.org/10.1016/J.MATLET.2020.127326

Carvalho, P. P., Wu, X., Yu, G., Dias, I. R., Gomes, M. E., Reis, R. L., & Gimble, J. M. (2011). The effect of storage time on adipose-derived stem cell recovery from human lipoaspirates. *Cells, Tissues, Organs, 194*(6), 494–500. https://doi.org/10.1159/000324892

Chahal, A. S., Gómez-Florit, M., Domingues, R. M. A., Gomes, M. E., & Tiainen, H. (2021). Human platelet lysate-loaded poly(ethylene glycol) hydrogels induce stem cell chemotaxis in vitro. *Biomacromolecules, 22*(8), 3486–3496. https://doi.org/10.1021/acs.biomac.1c00573

Chahal, A. S., Schweikle, M., Lian, A.-M., Reseland, J. E., Haugen, H. J., & Tiainen, H. (2020). Osteogenic potential of poly(ethylene glycol)-amorphous calcium phosphate composites on human mesenchymal stem cells. *Journal of Tissue Engineering, 11*, Article 204173142092684. https://doi.org/10.1177/2041731420926840

Dash, R., Foston, M., & Ragauskas, A. J. (2013). Improving the mechanical and thermal properties of gelatin hydrogels cross-linked by cellulose nanowhiskers. *Carbohydrate Polymers, 91*(2), 638–645. https://doi.org/10.1016/j.carbpol.2012.08.080

Domingues, R. M. A., Gomes, M. E., & Reis, R. L. (2014). The potential of cellulose nanocrystals in tissue engineering strategies. *Biomacromolecules, 15*(7), 2327–2346. https://doi.org/10.1021/bm500524s

Domingues, R. M. A., Silva, M., Gershovich, P., Betta, S., Babo, P., Caridade, S. G. Gomes, M. E., … (2015). Development of injectable hyaluronic acid/cellulose nanocrystals bionanocomposite hydrogels for tissue engineering applications. *Bioconjugate Chemistry, 26*(8), 1571–1581. https://doi.org/10.1021/acs.bioconjchem.5b00209

Fekete, N., Gadelorge, M., Frst, D., Maurer, C., Dausend, J., Fleury-Cappellesso, S. Rojewski, M. T., … (2012). Platelet lysate from whole blood-derived pooled platelet concentrates and apheresis-derived platelet concentrates for the isolation and expansion of human bone marrow mesenchymal stromal cells: Production process, content and identification of active comp. *Cytotherapy, 14*(5), 540–554. https://doi.org/10.3109/14653249.2012.655420

Ferreira, A. M., Gentile, P., Chiono, V., & Ciardelli, G. (2012). Collagen for bone tissue regeneration. *Acta Biomaterialia, 8*(9), 3191–3200. https://doi.org/10.1016/j.actbio.2012.06.014

Foster, E. J., Moon, R. J., Heux, L., Jean, B., Korey, M., Nieh, W., & Ong, K. J. (2018). Current characterization methods for cellulose nanomaterials. *Chemical Society Reviews, 47*(8), 2609–2679. https://doi.org/10.1039/c6cs00895j

Fragal, E. H., Cellet, T. S. P., Fragal, V. H., Companhoni, M. V. P., Ueda-Nakamura, T., Muniz, E. C.Rubira, A. F., … (2016). Hybrid materials for bone tissue engineering from biomimetic growth of hydroxiapatite on cellulose nanowhiskers. *Carbohydrate Polymers, 152*, 734–746. https://doi.org/10.1016/j.carbpol.2016.07.063

Fragal, E. H., Cellet, T. S. P., Fragal, V. H., Witt, M. A., Companhoni, M. V. P., Ueda-Nakamura, T.Rubira, A. F., … (2019). Biomimetic nanocomposite based on hydroxyapatite mineralization over chemically modified cellulose nanowhiskers: An active platform for osteoblast proliferation. *International Journal of Biological Macromolecules, 125*, 133–142. https://doi.org/10.1016/j.ijbiomac.2018.12.004

Gebauer, D., Oliynyk, V., Salajkova, M., Sort, J., Zhou, Q., Bergström, L., & Salazar-Alvarez, G. (2011). A transparent hybrid of nanocrystalline cellulose and amorphous calcium carbonate nanoparticles. *Nanoscale, 3*(9), 3563–3566. https://doi.org/10.1039/C1NR10681C

Gebauer, D., Völkel, A., & Cölfen, H. (2008). Stable prenucleation calcium carbonate clusters. *Science, 322*(5909), 1819–1822. https://doi.org/10.1126/SCIENCE.1164271

Gorski, J. P. (2011). Biomineralization of bone: A fresh view of the roles of non-collagenous proteins. *Frontiers in Bioscience, 16*(7), 2598–2621. https://doi.org/10.2741/3875

Hoppe, A., Güldal, N. S., & Boccaccini, A. R. (2011). A review of the biological response to ionic dissolution products from bioactive glasses and glass-ceramics. *Biomaterials, 32*(11), 2757–2774. https://doi.org/10.1016/j.biomaterials.2011.01.004

Hsieh, W. T., Liu, Y. S., Lee, Y. H., Rimando, M. G., Lin, K. H., & Lee, O. K. (2016). Matrix dimensionality and stiffness cooperatively regulate osteogenesis of mesenchymal stromal cells. *Acta Biomaterialia, 32*, 210–222. https://doi.org/10.1016/J.ACTBIO.2016.01.010

Huang, C., Bhagia, S., Hao, N., Meng, X., Liang, L., Yong, Q., & Ragauskas, A. J. (2019). Biomimetic composite scaffold from an in situ hydroxyapatite coating on cellulose nanocrystals. *RSC Advances, 9*(10), 5786–5793. https://doi.org/10.1039/C8RA09523J

Ishikawa, M., Oaki, Y., Tanaka, Y., Kakisawa, H., Salazar-Alvarez, G., & Imai, H. (2015). Fabrication of nanocellulose-hydroxyapatite composites and their application as water-resistant transparent coatings. *Journal of Materials Chemistry B, 3*(28), 5858–5863. https://doi.org/10.1039/c5tb00927h

Islam, M. S., Chen, L., Sisler, J., & Tam, K. C. (2018). Cellulose nanocrystal (CNC)–inorganic hybrid systems: Synthesis, properties and applications. *Journal of Materials Chemistry B, 6*(6), 864–883. https://doi.org/10.1039/C7TB03016A

Iwashita, N. (2016). X-ray powder diffraction. In *Materials Science and Engineering of Carbon* (pp. 7–25). Elsevier. https://doi.org/10.1016/B978-0-12-805256-3.00002-7.

Jakus, A. E., Rutz, A. L., Jordan, S. W., Kannan, A., Mitchell, S. M., Yun, C.Shah, R. N., … (2016). Hyperelastic "bone": A highly versatile, growth factor–free, osteoregenerative, scalable, and surgically friendly biomaterial. *Science Translational Medicine, 8*(358), 358ra127. https://doi.org/10.1126/scitranslmed.aaf7704

Khan, S., Siddique, R., Huanfei, D., Shereen, M. A., Nabi, G., Bai, Q.Bowen, H., … (2021). Perspective applications and associated challenges of using nanocellulose in treating bone-related diseases. *Frontiers in Bioengineering and Biotechnology, 9*, 350. https://doi.org/10.3389/FBIOE.2021.616555/BIBTEX

Kim, U. J., Kuga, S., Wada, M., Okano, T., & Kondo, T. (2000). Periodate oxidation of crystalline cellulose. *Biomacromolecules, 1*(3), 488–492. https://doi.org/10.1021/bm0000337

Klemm, D., Cranston, E. D., Fischer, D., Gama, M., Kedzior, S. A., Kralisch, D. Rauchfuß, F., … (2018). Nanocellulose as a natural source for groundbreaking applications in materials science: Today's state. *Materials Today, 21*(7), 720–748. https://doi.org/10.1016/j.mattod.2018.02.001

Komori, T. (2009). Regulation of bone development and extracellular matrix protein genes by RUNX2. *339*(1), 189–195. https://doi.org/10.1007/S00441-009-0832-8

Koons, G. L., Diba, M., & Mikos, A. G. (2020). Materials design for bone-tissue engineering. *Nature Reviews Materials, 5*(8), 584–603. https://doi.org/10.1038/s41578-020-0204-2

Kumar, A., Negi, Y. S., Choudhary, V., & Bhardwaj, N. K. (2014). Microstructural and mechanical properties of porous biocomposite scaffolds based on polyvinyl alcohol, nano-hydroxyapatite and cellulose nanocrystals. *Cellulose, 21*(5), 3409–3426. https://doi.org/10.1007/s10570-014-0339-7

Lian, J. B., Gravallese, E. M., & Stein, G. S. (2011). Osteoblasts and their signaling pathways: New frontiers for linkage to the immune system. *Osteoimmunology, 101–140*. https://doi.org/10.1016/B978-0-12-375670-1.10005-6

Londoño-Restrepo, S. M., Jeronimo-Cruz, R., Millán-Malo, B. M., Rivera-Muñoz, E. M., & Rodriguez-García, M. E. (2019). Effect of the nano crystal size on the X-ray diffraction patterns of biogenic hydroxyapatite from human, bovine, and porcine bones. *Scientific Reports, 9*(1), 1–12. https://doi.org/10.1038/s41598-019-42269-9

Lutolf, M. P., Gilbert, P. M., & Blau, H. M. (2009). Designing materials to direct stem-cell fate. *Nature, 462*(7272), 433–441. https://doi.org/10.1038/nature08602

Lynn, A. K., & Bonfield, W. (2005). A novel method for the simultaneous, titrant-free control of pH and calcium phosphate mass yield. *Accounts of Chemical Research, 38*(3), 202–207. https://doi.org/10.1021/AR040234D

Maeno, S., Niki, Y., Matsumoto, H., Morioka, H., Yatabe, T., Funayama, A.Tanaka, J., … (2005). The effect of calcium ion concentration on osteoblast viability, proliferation and differentiation in monolayer and 3D culture. *Biomaterials, 26*(23), 4847–4855. https://doi.org/10.1016/J.BIOMATERIALS.2005.01.006

Marie, P. J. (2010). The calcium-sensing receptor in bone cells: A potential therapeutic target in osteoporosis. *Bone, 46*(3), 571–576. https://doi.org/10.1016/J.BONE.2009.07.082

Mendes, B. B., Gómez-Florit, M., Araújo, A. C., Prada, J., Babo, P. S., Domingues, R. M. A. Gomes, M. E., … (2020). Intrinsically bioactive cryogels based on platelet lysate nanocomposites for hemostasis applications. *Biomacromolecules, 21*(9), 3678–3692. https://doi.org/10.1021/acs.biomac.0c00787

Mendes, B. B., Gómez-Florit, M., Babo, P. S., Domingues, R. M., Reis, R. L., & Gomes, M. E. (2018). Blood derivatives awaken in regenerative medicine strategies to modulate wound healing. *Advanced Drug Delivery Reviews, 129*, 376–393. https://doi.org/10.1016/j.addr.2017.12.018

Mendes, B. B., Gómez-Florit, M., Osório, H., Vilaça, A., Domingues, R. M. A., Reis, R. L., & Gomes, M. E. (2020). Cellulose nanocrystals of variable sulfation degrees can sequester specific platelet lysate-derived biomolecules to modulate stem cell response. *Chemical Communications, 56*(50), 6882–6885. https://doi.org/10.1039/D0CC01850C

Mendes, B. B., Gómez-Florit, M., Pires, R. A., Domingues, R. M. A., Reis, R. L., & Gomes, M. E. (2018). Human-based fibrillar nanocomposite hydrogels as bioinstructive matrices to tune stem cell behavior. *Nanoscale, 10*(36), 17388–17401. https://doi.org/10.1039/C8NR04273J

Moon, R. J., Martini, A., Nairn, J., Simonsen, J., & Youngblood, J. (2011). Cellulose nanomaterials review: Structure, properties and nanocomposites. *Chemical Society Reviews, 40*. https://doi.org/10.1039/c0cs00108b

Murphy, C. M., O'Brien, F. J., Little, D. G., & Schindeler, A. (2013). Cell-scaffold interactions in the bone tissue engineering triad. *European Cells and Materials, 26*, 120–132. https://doi.org/10.22203/eCM.v026a09

Niu, L., Jee, S. E., Jiao, K., Tonggu, L., Li, M., Wang, L., & Tay, F. R. (2016). Collagen intrafibrillar mineralization as a result of the balance between osmotic equilibrium and electroneutrality. *Nature Materials, 16*(3), 370–378. https://doi.org/10.1038/nmat4789

Nudelman, F., Pieterse, K., George, A., Bomans, P. H. H., Friedrich, H., Brylka, L. J. Sommerdijk, N. A. J. M., … (2010). The role of collagen in bone apatite formation in the presence of hydroxyapatite nucleation inhibitors. *Nature Materials, 9*(12), 1004–1009. https://doi.org/10.1038/nmat2875

Osborn, T. M., Helal, D., & Mehra, P. (2018). Iliac crest bone grafting for mandibular reconstruction: 10-year experience outcomes. *Journal of Oral Biology and Craniofacial Research, 8*(1), 25–29. https://doi.org/10.1016/j.jobcr.2017.12.001

Pina, S., Oliveira, J. M., & Reis, R. L. (2015). Natural-based nanocomposites for bone tissue engineering and regenerative medicine: A review. *Advanced Materials, 27*(7), 1143–1169. https://doi.org/10.1002/adma.201403354

Reznikov, N., Steele, J. A. M., Fratzl, P., & Stevens, M. M. (2016). A materials science vision of extracellular matrix mineralization. *Nature Reviews Materials, 1*(8), 16041. https://doi.org/10.1038/natrevmats.2016.41

Reznikov, N., Bilton, M., Lari, L., Stevens, M. M., & Kröger, R. (2018). Fractal-like hierarchical organization of bone begins at the nanoscale. *Science (New York, N.Y.), 360*(6388). https://doi.org/10.1126/science.aao2189

Rho, J. Y., Ashman, R. B., & Turner, C. H. (1993). Young's modulus of trabecular and cortical bone material: Ultrasonic and microtensile measurements. *Journal of Biomechanics, 26*(2), 111–119. https://doi.org/10.1016/0021-9290(93)90042-D

Schweikle, M., Bjørnøy, S. H., van Helvoort, A. T. J., Haugen, H. J., Sikorski, P., & Tiainen, H. (2019). Stabilisation of amorphous calcium phosphate in polyethylene glycol hydrogels. *Acta Biomaterialia, 90*, 132–145. https://doi.org/10.1016/j.actbio.2019.03.044

Si, J., Cui, Z., Wang, Q., Liu, Q., & Liu, C. (2016). Biomimetic composite scaffolds based on mineralization of hydroxyapatite on electrospun poly(ε-caprolactone)/nanocellulose fibers. *Carbohydrate Polymers, 143*, 270–278. https://doi.org/10.1016/j.carbpol.2016.02.015

Silva, C. R., Babo, P. S., Gulino, M., Costa, L., Oliveira, J. M., Silva-Correia, J. Gomes, M. E., … (2018). Injectable and tunable hyaluronic acid hydrogels releasing chemotactic and angiogenic growth factors for endodontic regeneration. *Acta Biomaterialia, 77*, 155–171. https://doi.org/10.1016/j.actbio.2018.07.035

Tang, Z., Li, X., Tan, Y., Fan, H., & Zhang, X. (2018). The material and biological characteristics of osteoinductive calcium phosphate ceramics. *Regenerative Biomaterials, 5*(1), 43–59. https://doi.org/10.1093/rb/rbx024

Tavares, M. T., Santos, S. C., Custódio, C. A., Farinha, J. P. S., Baleizão, C., & Mano, J. F. (2021). Platelet lysates-based hydrogels incorporating bioactive mesoporous silica nanoparticles for stem cell osteogenic differentiation. *Materials Today Bio, 9*, Article 100096. https://doi.org/10.1016/j.mtbio.2021.100096

Teixeira, S. P. B., Domingues, R. M. A., Shevchuk, M., Gomes, M. E., Peppas, N. A., & Reis, R. L. (2020). Biomaterials for sequestration of growth factors and modulation of cell behavior. *Advanced Functional Materials*. , Article 1909011. https://doi.org/10.1002/adfm.201909011

Terpos, E., & Gavriatopoulou, M. (2019). Multiple myeloma bone disease. In *, 329–340*. *Encyclopedia of endocrine diseases*. https://doi.org/10.1016/B978-0-12-801238-3.65375-8

Thrivikraman, G., Athirasala, A., Gordon, R., Zhang, L., Bergan, R., Keene, D. R. Bertassoni, L. E., … (2019). Rapid fabrication of vascularized and innervated cell-laden bone models with biomimetic intrafibrillar collagen mineralization. *Nature Communications, 10*(1). https://doi.org/10.1038/s41467-019-11455-8

Torgbo, S., & Sukyai, P. (2018). Bacterial cellulose-based scaffold materials for bone tissue engineering. *Applied Materials Today, 11*, 34–49. https://doi.org/10.1016/j.apmt.2018.01.004

Torgbo, S., & Sukyai, P. (2019). Fabrication of microporous bacterial cellulose embedded with magnetite and hydroxyapatite nanocomposite scaffold for bone tissue engineering. *Materials Chemistry and Physics, 237*, Article 121868. https://doi.org/10.1016/J.MATCHEMPHYS.2019.121868

van Kemenade, M. J. J. M., & de Bruyn, P. L. (1987). A kinetic study of precipitation from supersaturated calcium phosphate solutions. *Journal of Colloid and Interface Science, 118*(2), 564–585. https://doi.org/10.1016/0021-9797(87)90490-5

Viti, F., Landini, M., Mezzelani, A., Petecchia, L., Milanesi, L., & Scaglione, S. (2016). Osteogenic differentiation of MSC through calcium signaling activation: Transcriptomics and functional analysis. *PLOS ONE, 11*(2), Article e0148173. https://doi.org/10.1371/JOURNAL.PONE.0148173

Wang, L., & Nancollas, G. H. (2008). Calcium orthophosphates: Crystallization and dissolution. *Chemical Reviews, 108*(11), 4628–4669. https://doi.org/10.1021/CR0782574

Wang, W., & Yeung, K. W. K. (2017). Bone grafts and biomaterials substitutes for bone defect repair: A review. *Bioactive Materials, 2*(4), 224–247. https://doi.org/10.1016/j.bioactmat.2017.05.007

Wehmeyer, C., Naylor, A. J., Moeller, K., Poologasundarampillai, G., Pap, T., & Buckley, C. D. (2019). P124/O27 osteocyte-derived podoplanin is an important regulator of bone remodelling in the KBxN serum transfer model of rheumatoid arthritis. *Annals of the Rheumatic Diseases, 78*(Suppl. 1), A55–A56. https://doi.org/10.1136/ANNRHEUMDIS-2018-EWRR2019.112

Yamaguchi, A., Katagiri, T., Ikeda, T., Wozney, J. M., Rosen, V., Wang, E. A.Yoshiki, S., … (1991). Recombinant human bone morphogenetic protein-2 stimulates osteoblastic maturation and inhibits myogenic differentiation in vitro. *Journal of Cell Biology, 113*(3), 681–687. https://doi.org/10.1083/jcb.113.3.681

Ye, Z., Zhu, X., Mutreja, I., Boda, S. K., Fischer, N. G., Zhang, A.Aparicio, C., … (2021). Biomimetic mineralized hybrid scaffolds with antimicrobial peptides. *Bioactive Materials, 6*(8), 2250–2260. https://doi.org/10.1016/j.bioactmat.2020.12.029

Yu, L., & Wei, M. (2021). Biomineralization of collagen-based materials for hard tissue repair. *International Journal of Molecular Sciences, 22*(2), 944. https://doi.org/10.3390/IJMS22020944

Zhang, Q., Lu, H., Kawazoe, N., & Chen, G. (2014). Pore size effect of collagen scaffolds on cartilage regeneration. *Acta Biomaterialia, 10*(5), 2005–2013. https://doi.org/10.1016/j.actbio.2013.12.042

Zhang, Q., Yang, T., Zhang, R., Liang, X., Wang, G., Tian, Y.Tian, W., … (2021). Platelet lysate functionalized gelatin methacrylate microspheres for improving angiogenesis in endodontic regeneration. *Acta Biomaterialia*. https://doi.org/10.1016/j.actbio.2021.09.024